

NATIONAL AERONAUTICS AND SPACE ADMINISTRATION

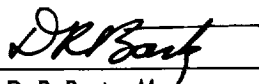
*Technical Report 32-987*

*Acceleration of Liquids in  
Two-Phase Nozzles*

*D. G. Elliott*

*E. Weinberg*

Approved by:



---

D. R. Bartz, Manager  
Research and Advanced Concepts Section

JET PROPULSION LABORATORY  
CALIFORNIA INSTITUTE OF TECHNOLOGY  
PASADENA, CALIFORNIA

July 1, 1968

**TECHNICAL REPORT 32-987**

**Copyright © 1968  
Jet Propulsion Laboratory  
California Institute of Technology  
Prepared Under Contract No. NAS 7-100  
National Aeronautics & Space Administration**

### **Acknowledgment**

Important contributions were made by several people. L. G. Hays performed the one-component nozzle analysis. D. J. Cerini conducted the nitrogen-water tests on the 50-in. nozzle. H. Otte conducted the Freon-water tests. The computer programs were developed by C. Milton, B. Williams, A. Voskressensky, and P. Kaestner.

# Contents

<b>I. Introduction</b>	1
<b>II. Analysis</b>	2
A. Two-Component Flow	3
1. Assumptions	3
2. Derivation of equations for free-stream flow	3
3. Optimum pressure profile	10
4. Wall shear and boundary layer	11
5. Auxiliary quantities	12
6. Units	14
B. One-Component Flow	14
1. Assumptions	14
2. Derivation of equations for free-stream flow	14
3. Optimum pressure profile	15
4. Wall shear and boundary layer	15
5. Auxiliary quantities	15
6. Units	15
C. Isentropic Flow	15
1. Two-component flow	15
2. One-component flow	16
<b>III. Computer Programs</b>	16
<b>IV. Two-Phase Nozzle Design</b>	16
<b>V. Comparison with Experiment</b>	21
A. Nitrogen–Water Tests in the 50-in. Nozzle	21
1. Construction and test procedure	21
2. Pressure profile	27
3. Flow rate	28
4. Exit velocity	29
B. Freon–Water Experiment	29
1. Flow rate	29
2. Exit velocity	29
C. Six-Inch Nozzle	32
1. Flow rate	32
2. Exit velocity	32

## Contents (contd)

D. Steam Nozzle . . . . .	33
E. Liquid Nitrogen Nozzle . . . . .	34
<b>VI. Summary and Conclusions . . . . .</b>	<b>34</b>
<b>Nomenclature . . . . .</b>	<b>35</b>
<b>References . . . . .</b>	<b>41</b>

## Tables

1. Conversion factors employed in computer programs . . . . .	14
2. Theoretical performance of 50-in. nozzle with water and nitrogen . . . . .	28
3. Measured performance of 50-in. nozzle with water and nitrogen . . . . .	30
4. Theoretical and measured performance of 50-in. nozzle with water and Freon 1301 at 150 psia . . . . .	30

## Figures

1. Two-phase nozzle flow geometry and nomenclature . . . . .	2
2. Drag coefficient of spheres and drops . . . . .	9
3. Annular nozzle geometry . . . . .	13
4. Correspondence between nozzle length and Lagrangian multiplier . . . . .	17
5. Normalized profiles of optimum nozzles . . . . .	18
6. Modification of optimum shape to obtain experimental nozzle . . . . .	18
7. Theoretical pressure profile for experimental nozzle and tabulated values employed in real-flow analysis . . . . .	19
8. Effect of length and initial drop diameter on exit velocity, with and without breakup . . . . .	19
9. Variation of drop diameter with distance from inlet . . . . .	19
10. Variation of drop diameter with travel time . . . . .	20
11. Effect of nozzle length and flow rate on exit velocity with friction . . . . .	20
12. Optimum and off-optimum pressure profiles and corresponding exit velocities . . . . .	20
13. Variation of liquid and gas velocities with distance . . . . .	21
14. Variation of liquid and gas temperatures with distance . . . . .	21
15. Variation of void fraction with distance . . . . .	21

## Contents (contd)

### Figures (contd)

16. 50-in. nozzle and injector . . . . .	22
17. Injection orifice details . . . . .	23
18. Experimental nozzle in operation . . . . .	24
19. Exit jet at 1.0- $\mu$ s exposure . . . . .	25
20. Water injection pressure drop . . . . .	26
21. Nitrogen injection pressure drop . . . . .	26
22. Freon injection pressure drop . . . . .	26
23. Comparison of theoretical and experimental pressure profiles . . . . .	27
24. Comparison of theoretical and experimental variation of pressure with mixture ratio 21 in. upstream of exit . . . . .	27
25. Comparison of theoretical and experimental variation of pressure with mixture ratio at exit . . . . .	27
26. Comparison of theoretical and experimental flow rates at 150-psia nozzle inlet pressure . . . . .	28
27. Comparison of theoretical and experimental flow rates at 190-psia nozzle inlet pressure . . . . .	29
28. Comparison of theoretical and experimental flow rates at 230-psia nozzle inlet pressure . . . . .	29
29. Comparison of theoretical and experimental exit velocities at 150-psia nozzle inlet pressure . . . . .	31
30. Comparison of theoretical and experimental exit velocities at 190-psia nozzle inlet pressure . . . . .	31
31. Comparison of theoretical and experimental exit velocities at 230-psia nozzle inlet pressure . . . . .	31
32. Comparison of theoretical and experimental flow rates using Freon . . . . .	31
33. Comparison of theoretical and experimental exit velocities using Freon . . . . .	32
34. 6-in. nozzle and injector . . . . .	32
35. Comparison of theoretical and experimental flow rates for 6-in. nozzle . . . . .	33
36. Comparison of theoretical and experimental exit velocities for 6-in. nozzle . . . . .	33
37. Comparison of theoretical and experimental flow rates for steam-water nozzle of Ref. 28 . . . . .	33
38. Comparison of theoretical and experimental exit velocities for liquid nitrogen nozzle of Ref. 29 . . . . .	34

## **Abstract**

Two-phase nozzle flow of liquid drops mixed with a gas is analyzed for both the one-component and the two-component cases. Drop volume, drop breakup and vaporization, variable fluid properties, and solubility of the gas in the liquid are taken into account. Computer programs employing the analysis provide gas and liquid velocities and temperatures, as well as drop diameter, as a function of distance through a nozzle when initial conditions and fluid properties are specified. Wall shear and boundary-layer growth are also computed, and an option provides the optimum (maximum exit velocity for given length) nozzle contour. Calculations for typical fluids illustrate the effect on nozzle exit velocity of nozzle contour and length, initial drop size, mixture ratio, and pressure ratio. Nozzle experiments with nitrogen-water mixtures and Freon-water mixtures show that actual velocities and flow rates agree with the analysis within 5%.





# Acceleration of Liquids in Two-Phase Nozzles

## I. Introduction

High-velocity liquids are a source of power for pumping (Refs. 1 and 2) and for magnetohydrodynamic (MHD) electrical power generation (Refs. 3 and 4). Liquid velocities of 300 to 1000 ft/s are employed in these applications, and the velocities are produced by accelerating the liquids in two-phase nozzles.

A two-phase nozzle is a nozzle in which a liquid and a gas are mixed at high pressure and low velocity and expanded to low pressure and high velocity. The gas phase may either be the vapor of the liquid being accelerated, in which case the flow is termed "one-component," or a different chemical species from the liquid, in which case the flow is termed "two-component." A one-component fluid combination of interest for MHD power generation is potassium and potassium vapor; one-component combinations that have been investigated experimentally are water and steam, and liquid nitrogen and nitrogen. The fluid combination of greatest interest for MHD power generation is the two-component combination of liquid lithium and cesium vapor. The two-component combination which has been most extensively investigated experimentally is water mixed with nitrogen or air.

Typical of the nozzle flow conditions for MHD power generation are the following, calculated for a 50-in.-long cesium-lithium nozzle designed to be employed in an MHD system of 300 kW electric output (Ref. 4). Conditions at the nozzle inlet are: pressure, 137 psia; temperature, 1800°F; velocity, 50 ft/s; void fraction, 0.72; liquid flow rate, 186 lb/s (180 lb/s Li and 6 lb/s dissolved Cs); gas flow rate (Cs vapor), 14 lb/s; and liquid drop diameter large enough (say, 0.05 in.) to result in breakup in the nozzle. Conditions at the exit are: pressure, 15 psia; liquid temperature, 1790°F; gas temperature, 1610°F; liquid velocity, 495 ft/s; gas velocity, 687 ft/s; void fraction, 0.96; liquid flow rate, 181 lb/s (180 lb/s Li and 1 lb/s dissolved Cs); gas flow rate, 19 lb/s; and liquid drop diameter, 0.019 in. The nozzle is converging-diverging, a requirement resulting from the low sonic velocity in two-phase mixtures, with a throat diameter of 4.8 in. and an exit diameter of 7.8 in.

It will be shown in this report that the exit velocities of the nozzles of interest for MHD power generation can be calculated to an accuracy of 5% given the properties of the fluids. This accuracy is possible because the nozzles employ spatially uniform mixing of the liquid and gas at the nozzle inlet and are long and slender, making the

one-dimensional equations for two-phase flow closely applicable. The only approximation needed is in determining drop diameter, and the method adopted for calculating this diameter is adequate for 5% accuracy in calculated exit velocity.

Tangren, Dodge, and Seifert (Ref. 5) derived the equations for isentropic flow of an immiscible two-component mixture with equal temperatures of the liquid and the gas. The first extensive experiments on two-phase nozzles were reported by Elliott (Ref. 1), who found that actual nozzles achieve 80 to 90% of the isentropic exit velocity.

The differential equations for two-phase flow with velocity and temperature differences between the phases were derived by Kliegel (Ref. 6). Those equations were successfully applied by Kliegel and others to gas-solid flows in rocket motor nozzles, a situation in which the particle sizes are known. The fact that particle sizes can also be determined for a gas-liquid nozzle was pointed out by Crabtree (Ref. 7). He showed that the flow conditions of the drops in a two-phase nozzle are such that the drops will break up early in the acceleration process, and he suggested calculating the resulting diameter from the Weber number = 6 criterion, which correlates the data for atomization by gas streams within a factor of about two. An uncertainty in drop diameter of this magnitude causes only about a 3% uncertainty in nozzle exit velocity. The  $We = 6$  criterion was incorporated into a two-phase nozzle computer program by Netzer (Ref. 8), and the computed exit velocities agreed within 3% with measured values in a short air-water nozzle, where friction would be expected to be small. A long nozzle, in which friction would be expected to be significant, gave velocities 25% below the prediction.

Netzer's analysis employed equal phase temperatures, and this approximation was eliminated in an analysis by Elliott (Ref. 9) which accounted for both the velocity difference and temperature difference between the phases, while again employing the  $We = 6$  criterion for drop breakup. The analysis of Ref. 9 gave nozzle exit velocities that agreed within 5% with measurements on a large nitrogen-water nozzle.

This report describes the final version of the computation method reported in Ref. 9. The effects added were friction, mass transfer between phases through vaporization and condensation, variable properties, solubility of the gas in the liquid, and finite vapor pressure of the liquid. The analysis retained the basic assumption of one-

dimensional flow. A procedure for determining the optimum nozzle shape was added, and the one-component flow case was analyzed.

## II. Analysis

The problem analyzed is illustrated in Fig. 1. A spatially uniform one- or two-component mixture of liquid drops and gas enters a nozzle at high pressure and low velocity and expands to low pressure and high velocity. The objective of the analysis is to determine, for a specified pressure profile  $p(x)$ , the drop diameter  $D$  and the temperatures  $T_g$  and  $T_l$ , velocities  $V_g$  and  $V_l$ , and flow rates  $\dot{m}_g$  and  $\dot{m}_l$  of the gas and liquid phases, respectively, at each station in the nozzle, given the initial values of  $D$ ,  $T_g$ ,  $T_l$ ,  $V_g$ ,  $V_l$ , the total flow rate, and the properties of the fluids.

The five relations employed to compute the five unknowns  $D$ ,  $T_g$ ,  $T_l$ ,  $V_g$ , and  $V_l$  are (1) the momentum equation for the mixture, (2) the energy equation for the mixture, (3) the drop drag equation, (4) the drop heat-transfer equation, and (5) the drop breakup criterion.

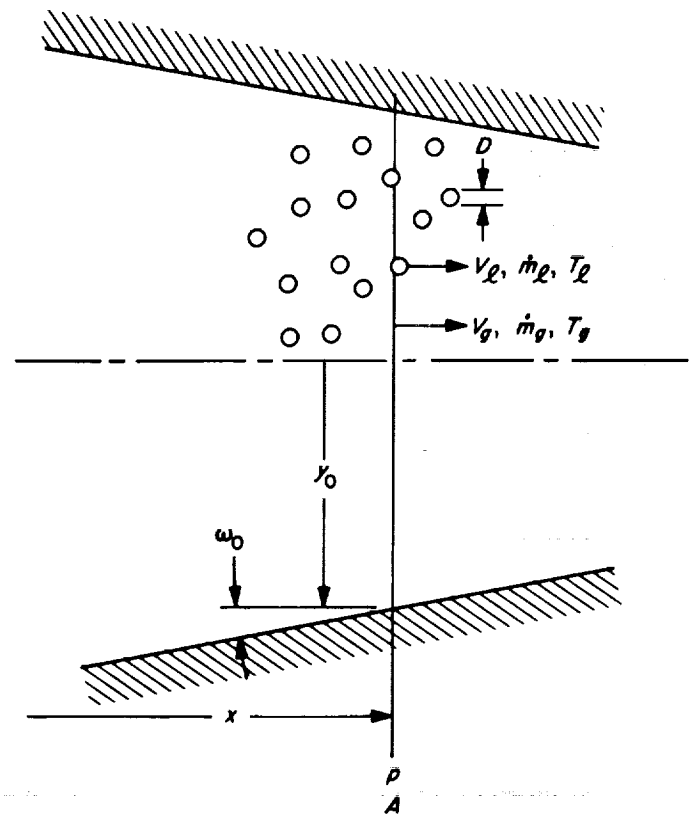


Fig. 1. Two-phase nozzle flow geometry and nomenclature

Solubility and vapor pressure relations provide the flow rate ratio  $\dot{m}_g/\dot{m}_l$ .

## A. Two-Component Flow

1. **Assumptions.** The assumptions employed in the two-component analysis are as follows:

1. The liquid is uniformly dispersed as spherical drops, all of the same diameter.
2. The drops break up to limit the Weber number to 6.
3. There are no external forces acting on the two-phase mixture other than pressure and wall shear, and there is no heat transfer to or from the mixture.
4. The flow is one-dimensional.
5. The drops are large enough for the surface curvature to have negligible effect on the vapor pressure of the liquid and for the surface energy to be negligible.
6. The drops are isothermal.
7. The gas mixture obeys the additive-pressure law.
8. The partial pressure of the predominantly liquid component is given by Raoult's Law.
9. The concentration of the predominantly gaseous component in the liquid is given by Henry's Law.
10. The volume of the liquid solution is equal to the sum of the volumes of the pure liquids.

Assumption 1 restricts the analysis to nozzles having spatially uniform injection of the liquid into the gas and operating at gas-to-liquid volume ratios greater than unity. Assumption 2, the drop breakup criterion, states that drop diameter is limited to a value  $D$  for which  $We = \rho_g V_s^2 D / 2\sigma = 6$ . Thus,

$$D_{\max} = \frac{12\sigma}{\rho_g V_s^2} \quad (1)$$

where  $\rho_g$  is the gas density,  $V_s$  is the slip velocity  $V_g - V_l$ , and  $\sigma$  is the liquid surface tension. The form of Eq. (1) is physically reasonable in that the Weber number is proportional to the ratio of stagnation pressure  $\rho_g V_s^2 / 2$  to surface tension pressure  $4\sigma/D$ . Hence, a drop would be expected to flatten and break up at a sufficiently high value of  $We$ . This has been verified experimentally (Refs. 10 and 11) and the critical Weber number found to be 6, within a factor of 2. An additional restriction is that for actual breakup to occur, the time spent at a Weber number exceeding 6 must be longer than the natural period of oscillation of the drop,  $\pi(\rho_l D^3/\sigma)^{1/2}/4$ , where  $\rho_l$  is the

density of the liquid (Ref. 11). As shown later, this requirement is met only in two-phase nozzles longer than about 10 in., and Assumption 2 may cause the analysis to overestimate the exit velocity by increasing amounts as the nozzle length decreases below 10 in.

Assumption 3 excludes magnetohydrodynamic and mechanical body forces. The exclusion of wall heat transfer is correct for the insulated nozzles of interest for power systems.

Assumption 4 is closely met in practical nozzles since good performance requires small wall angles, large throat radius of curvature, and uniformly distributed injection of the fluids at the nozzle entrance.

Assumption 5 is valid for the drop sizes of 0.001 to 0.010 in. produced by the Eq. (1) breakup criterion. Assumption 6 is valid because of the rapid internal circulation in drops (Ref. 12). Assumption 7 introduces negligible error in most cases of practical interest since the vapor pressure of the liquid is small and need only be evaluated approximately.

Assumptions 8, 9, and 10 are either valid, or cause little error, for fluids of low miscibility, which are the fluids of interest for power systems.

## 2. Derivation of equations for free-stream flow

a. **Continuity.** Referring to Fig. 1, the nozzle flow area  $A$  is equal to the gas flow area  $\dot{m}_g/\rho_g V_g$  plus the liquid flow area  $\dot{m}_l/\rho_l V_l$ . Thus,

$$A = \dot{m}_g \left( \frac{1}{\rho_g V_g} + \frac{r}{\rho_l V_l} \right) \quad (2)$$

where  $r$  is the mass mixture ratio  $\dot{m}_l/\dot{m}_g$ .

b. **Momentum.** By Assumption 3, the only force acting on the free-stream flow is that due to the pressure gradient. If  $\dot{M}$  is the momentum flux at flow area  $A$ , the change in momentum flux across pressure increment  $dp$  is

$$d\dot{M} = -A dp \quad (3)$$

The momentum flux can be written as the sum of the momentum fluxes of the gas and liquid. Thus,

$$\dot{M} = \dot{m}_g V_g + \dot{m}_l V_l \quad (4)$$

If the flow were allowed to continue at constant pressure,  $V_g$  and  $V_l$  would become equal to each other at the

mass-weighted mean velocity  $\bar{V}$ . Since, for this process,  $d\dot{M} = 0$ , the value of  $\bar{V}$  is given by

$$(\dot{m}_g + \dot{m}_l)\bar{V} = \dot{m}_g V_g + \dot{m}_l V_l \quad (5)$$

or

$$\bar{V} = \frac{V_g + rV_l}{1 + r} \quad (6)$$

Thus, the momentum flux can be written

$$\dot{M} = (\dot{m}_g + \dot{m}_l)\bar{V} \quad (7)$$

Since  $\dot{m}_g + \dot{m}_l$  is constant, the change in momentum flux is

$$d\dot{M} = (\dot{m}_g + \dot{m}_l)d\bar{V} \quad (8)$$

Substituting Eqs. (8) and (2) into Eq. (3),  $d\bar{V}$  can be written

$$d\bar{V} = -\frac{1}{1+r} \left( \frac{1}{\rho_g V_g} + \frac{r}{\rho_l V_l} \right) dp \quad (9)$$

The slip ratio is defined as

$$s = V_g/\bar{V} = (V_g - V_l)/\bar{V} \quad (10)$$

This equation can be combined with Eq. (6) to give  $V_g$  and  $V_l$  in terms of  $\bar{V}$ :

$$V_g = \left( 1 + \frac{rs}{1+r} \right) \bar{V} = a\bar{V} \quad (11)$$

$$V_l = \left( 1 - \frac{s}{1+r} \right) \bar{V} = b\bar{V} \quad (12)$$

The gas density can be expressed as

$$\rho_g = W_g p / RT_g \quad (13)$$

where  $W_g$  is the effective molecular weight of the gas mixture and  $R$  is the universal gas constant. Equation (13) is the definition of the effective molecular weight  $W_g$ , which is the quantity that gives the actual gas density when substituted in Eq. (13).

Substituting Eqs. (11)–(13) into Eq. (9), the differential momentum equation is

$$2\bar{V}d\bar{V} = d\bar{V}^2 = -\frac{2}{1+r} \left( \frac{RT_g}{aW_g p} + \frac{r}{b\rho_l} \right) dp \quad (14)$$

A semi-integrated form of this equation can be written which permits a larger step size in numerical integration. The quantities  $a$  and  $b$  are slowly varying because  $s$  is typically only 0.1 to 0.3 and slowly varying. The quantities  $r$ ,  $T_g$ ,  $W_g$  and  $\rho_l$  are also slowly varying. Integrating Eq. (14) over a pressure increment  $\Delta p$ , for which  $a$ ,  $b$ ,  $r$ ,  $T_g$ ,  $W_g$ , and  $\rho_l$  are constant to within the desired accuracy, the change in  $\bar{V}^2$  is

$$\Delta\bar{V}^2 = -\int_{p-\frac{\Delta p}{2}}^{p+\frac{\Delta p}{2}} \frac{2}{1+r} \left( \frac{RT_g}{aW_g p} + \frac{r}{b\rho_l} \right) dp \quad (15)$$

All quantities other than pressure can be taken outside the integral and evaluated at their mean values (denoted by subscript  $m$ ) corresponding to the mid-interval pressure  $p$ . Thus,

$$\Delta\bar{V}^2 = -\frac{2}{1+r_m} \times \left( \frac{RT_{g_m}}{a_m W_{g_m}} \int_{p-\frac{\Delta p}{2}}^{p+\frac{\Delta p}{2}} \frac{dp}{p} + \frac{r_m}{b_m \rho_{l_m}} \int_{p-\frac{\Delta p}{2}}^{p+\frac{\Delta p}{2}} dp \right) \quad (16)$$

Performing the integrations,

$$\Delta\bar{V}^2 = -\frac{2}{1+r_m} \left( \frac{RT_{g_m}}{a_m W_{g_m}} \log_e \frac{p+\Delta p/2}{p-\Delta p/2} + \frac{r_m \Delta p}{b_m \rho_{l_m}} \right) \quad (17)$$

Equation (17) is the final form of the momentum equation.

*c. Energy.* The enthalpy change of the mixture between state 1 (the beginning of pressure interval  $\Delta p$ ) and state 2 (the end of the interval) can be evaluated in two steps: (1) phase change at  $p_1$ ,  $T_{g1}$ ,  $T_{l1}$  and (2) change to  $p_2$ ,  $T_{g2}$ ,  $T_{l2}$ , at fixed composition.

The enthalpy change for step 1 is

$$\begin{aligned} \Delta H_1 = & \left( \text{amount of A} \right) \times \left( \begin{array}{l} \text{enthalpy required} \\ \text{to vaporize and} \\ \text{heat unit mass of} \\ \text{A from } T_{l_1} \text{ to } T_{g_1} \end{array} \right) \\ & + \left( \text{amount of B} \right) \times \left( \begin{array}{l} \text{enthalpy required} \\ \text{to vaporize and} \\ \text{heat unit mass of} \\ \text{B from } T_{l_1} \text{ to } T_{g_1} \end{array} \right) \\ & + \left( \text{amount of A and} \right) \times \left( \begin{array}{l} \text{kinetic energy} \\ \text{required to} \\ \text{accelerate unit mass} \\ \text{from } V_{l_1} \text{ to } V_{g_1} \end{array} \right) \\ & \left( \text{B vaporized} \right) \end{aligned}$$

or

$$\begin{aligned} \Delta H_1 = & (\dot{m}_{a_{g_2}} - \dot{m}_{a_{g_1}}) [L_{a_1} + c_{a_{g_1}} (T_{g_1} - T_{l_1})] \\ & + (\dot{m}_{b_{g_2}} - \dot{m}_{b_{g_1}}) [L_{b_1} + c_{b_{g_1}} (T_{g_1} - T_{l_1})] \\ & + (\dot{m}_{g_2} - \dot{m}_{g_1}) (V_{g_1}^2 - V_{l_1}^2) / 2 \end{aligned} \quad (18)$$

where  $L$  and  $c$  are latent heat and specific heat, respectively.

Introducing more compact notation,

$$\begin{aligned} \Delta H_1 = & \Delta \dot{m}_{a_g} (L_{a_1} + c_{a_{g_1}} \delta_1 T) \\ & + \Delta \dot{m}_{b_g} (L_{b_1} + c_{b_{g_1}} \delta_1 T) + \frac{\Delta \dot{m}_g \delta_1 V^2}{2} \end{aligned} \quad (19)$$

The enthalpy change for step 2 is evaluated from the temperature, pressure, and velocity changes, with properties evaluated at mean  $T$  and  $p$  for the interval.

$$\begin{aligned} \Delta H_2 = & \dot{m}_{g_2} [c_{g_m} (T_{g_2} - T_{g_1}) + \frac{1}{2} (V_{g_2}^2 - V_{g_1}^2)] \\ & + \dot{m}_{l_2} [c_{l_m} (T_{l_2} - T_{l_1}) + \frac{p_2 - p_1}{\rho_{l_m}} \\ & + \frac{1}{2} (V_{l_2}^2 - V_{l_1}^2)] \end{aligned} \quad (20)$$

$$\begin{aligned} = & \dot{m}_{g_2} \left( c_{g_m} \Delta T_g + \frac{\Delta V_g^2}{2} \right) \\ & + \dot{m}_{l_2} \left( c_{l_m} \Delta T_l + \frac{\Delta p}{\rho_{l_m}} + \frac{\Delta V_l^2}{2} \right) \end{aligned} \quad (21)$$

By Assumption 3, no work is done by the free-stream flow and no heat is transferred to it. Hence,

$$\Delta H_1 + \Delta H_2 = 0 \quad (22)$$

Substituting Eqs. (19) and (21) into Eq. (22) and solving for  $\Delta T_g$  gives the energy equation for the mixture:

$$\begin{aligned} \Delta T_g = & - \frac{1}{c_{g_m}} \left[ \frac{\Delta V_g^2}{2} + r_2 \left( c_{l_m} \Delta T_l + \frac{\Delta p}{\rho_{l_m}} + \frac{\Delta V_l^2}{2} \right) \right. \\ & + \frac{\Delta \dot{m}_g \delta_1 V^2}{2 \dot{m}_{g_2}} + \frac{\Delta \dot{m}_{a_g}}{\dot{m}_{g_2}} \left( L_{a_1} + c_{a_{g_1}} \delta_1 T \right) \\ & \left. + \frac{\Delta \dot{m}_{b_g}}{\dot{m}_{g_2}} \left( L_{b_1} + c_{b_{g_1}} \delta_1 T \right) \right] \end{aligned} \quad (23)$$

*d. Drag.* Although no force other than pressure acts on the free-stream flow as a whole, a drag force exists between the phases. Hence, a second momentum equation must be written using as the control volume the boundary between the phases.

The two forces acting on each liquid drop are the buoyancy due to the pressure gradient and the drag due to the relative gas velocity. The sum of these is equal to the mass times the acceleration of the drop. Thus, for a single drop,

$$\begin{aligned} & \left( \text{dynamic pressure of} \right) \times \left( \text{drag} \right) \times \left( \text{frontal area} \right) \\ & \left( \text{relative gas flow} \right) \times \left( \text{coefficient} \right) \times \left( \text{of drop} \right) \\ & - \left( \text{volume} \right) \times \left( \text{pressure} \right) = \left( \text{mass} \right) \times \left( \text{acceleration} \right) \\ & \left( \text{of drop} \right) \times \left( \text{gradient} \right) = \left( \text{of drop} \right) \times \left( \text{of drop} \right) \end{aligned}$$

or

$$\begin{aligned} & \left( \frac{1}{2} \rho_g |V_s| V_s \right) C_D \frac{\pi D^2}{4} - \frac{\pi D^3}{6} \frac{dp}{dx} \\ & = \left( \frac{\pi D^3}{6} \rho_l \right) \left( V_l \frac{dV_l}{dx} \right) \end{aligned} \quad (24)$$

The absolute value sign in the first term makes the drag force positive when  $V_g > V_l$  and negative when  $V_g < V_l$ .

Solving Eq. (24) for  $dV_l$ ,

$$dV_l = \frac{3 \rho_g |s| s \bar{V}^2 C_D dx}{4 \rho_l V_l D} - \frac{dp}{\rho_l V_l} \quad (25)$$

Differentiating Eq. (12),  $dV_l$  can also be expressed in terms of  $s$ ,  $r$ , and  $\bar{V}$ . Thus,

$$dV_l = b d\bar{V} + \bar{V} \left[ \frac{s dr}{(1+r)^2} - \frac{ds}{1+r} \right] \quad (26)$$

Solving for  $ds$ ,

$$ds = \frac{b(1+r) d\bar{V}}{\bar{V}} + \frac{s dr}{1+r} - \frac{(1+r) dV_l}{\bar{V}} \quad (27)$$

Substituting  $dV_l$  from Eq. (25), noting that  $d\bar{V} = d\bar{V}^2/2\bar{V}$ , using Eq. (12), and writing for a finite increment,

$$\Delta s = \frac{b_m(1+r_m) \Delta \bar{V}^2}{2\bar{V}_m^2} + \frac{(1+r_m) \Delta p}{b_m \rho_{l_m} \bar{V}_m^2} + \frac{s_m \Delta r}{1+r_m} - \frac{3\rho_{g_m} |s_m| s_m C_{D_m} (1+r_m) \Delta x}{4 b_m \rho_{l_m} D} \quad (28)$$

This is the drag equation employed when  $x$  is specified as a function of  $p$ . In a later section, the problem will be changed to find the optimum value of  $\Delta s$  and then the corresponding value of  $\Delta x$ . Solving Eq. (28) for  $\Delta x$  yields the required alternative equation:

$$\Delta x = \frac{4D}{3\rho_{g_m} |s_m| s_m C_{D_m} \bar{V}_m^2} \left[ \Delta p + \frac{b_m^2 \rho_{l_m} \Delta \bar{V}^2}{2} + \frac{b_m \rho_{l_m} \bar{V}_m^2}{1+r_m} \left( \frac{s_m \Delta r}{1+r_m} - \Delta s \right) \right] \quad (29)$$

*e. Heat transfer.* Although no heat is transferred to the mixture as a whole, heat transfer exists between the phases. Hence, a second energy equation must be written using as the control volume the boundary between the phases.

The work  $dW$  done on the liquid is that due to drag by the gas. (Only work done by shear or shaft forces is included in  $dW$  when writing the First Law for a control volume, as shown in Ref. 13, p. 39.) Multiplying Eq. (24) by the number flow rate of drops  $\dot{N} = 6\dot{m}_l/\pi D^3 \rho_l$ , the drag force  $F_d$  on that quantity of liquid is

$$F_d = \frac{\dot{N}}{8} \rho_g |V_s| V_s C_{D_m} \pi D^2 = \frac{\dot{m}_l}{\rho_l} \frac{dp}{dx} + \dot{m}_l V_l \frac{dV_l}{dx} \quad (30)$$

The work done on the liquid is

$$-dW = F_d dx = \dot{m}_l \left( \frac{dp}{\rho_l} + \frac{dV_l^2}{2} \right) \quad (31)$$

The heat  $dQ$  transferred from the liquid is made up of two parts: (1) the convective cooling due to the temperature difference between the liquid and gas and (2) the

evaporative cooling due to the latent heat supplied to the liquid vaporized. The convective cooling is

$$-dQ_c = h A_d \dot{N} (T_l - T_g) dt \quad (32)$$

where  $h$  is the heat-transfer coefficient,  $A_d = \pi D^2$  is the surface area of a drop, and  $dt = dx/V_l$  is the time required to traverse  $dx$ . Thus,

$$-dQ_c = \frac{6h\dot{m}_l (T_g - T_l) dx}{D \rho_l V_l} \quad (33)$$

The evaporative cooling is

$$-dQ_v = L_a d\dot{m}_{a_g} + L_b d\dot{m}_{b_g} \quad (34)$$

The change in enthalpy of the liquid over the pressure increment  $dp$  is

$$dH = \dot{m}_l \left( c_l dT_l + \frac{dp}{\rho_l} + \frac{dV_l^2}{2} \right) \quad (35)$$

Substituting Eqs. (31), (33), (34), and (35) into the steady-flow energy equation  $dQ - dW = dH$ , the result is

$$\frac{6h\dot{m}_l \delta T dx}{D \rho_l V_l} - L_a d\dot{m}_{a_g} - L_b d\dot{m}_{b_g} = \dot{m}_l c_l dT_l \quad (36)$$

where  $\delta T = T_g - T_l$ .

Writing for a finite interval, the final form of the drop heat-transfer equation is

$$\Delta T_l = \frac{1}{c_{l_m}} \left[ \frac{6h\delta_m T \Delta x}{D \rho_{l_m} \bar{V}_{l_m}} - L_{a_m} \frac{\Delta \dot{m}_{a_g}}{\dot{m}_{l_m}} - L_{b_m} \frac{\Delta \dot{m}_{b_g}}{\dot{m}_{l_m}} \right] \quad (37)$$

Equations (1), (17), (23), (28), and (37) are the five equations that must be solved simultaneously to obtain the values of the five dependent variables  $D$ ,  $T_g$ ,  $T_l$ ,  $V_g$ , and  $V_l$  as a function of the independent variable  $p$ . To carry out the solution, all quantities in the equations must be expressed in terms of these six variables. The additional equations required will be developed next.

*f. Phase properties.* By Assumption 9, the mole fraction of component A in the liquid is proportional to the partial pressure  $p_a$  of component A (Henry's Law, Ref. 14, p. 181). Thus,

$$\frac{\dot{m}_{a_l}/W_{a_l}}{\dot{m}_{a_l}/W_{a_l} + (\dot{m}_l - \dot{m}_{a_l})/W_{b_l}} = Hp_a \quad (38)$$

where  $\dot{m}_{a_l}$  is the flow rate of dissolved component A,  $W_{a_l}$  and  $W_{b_l}$  are the molecular weights of liquid A and B, respectively, and  $H$  is the mole fraction dissolved per unit pressure of A.

Solving for  $\dot{m}_{a_l}/\dot{m}_l = \alpha$  yields

$$\alpha = \frac{(W_{a_l}/W_{b_l}) Hp_a}{1 + (W_{a_l}/W_{b_l} - 1) Hp_a} \quad (39)$$

By Assumption 8, the partial pressure  $p_b$  of component B is equal to the vapor pressure  $p_{b_0}$  of pure B multiplied by the mole fraction of B in the liquid (Raoult's Law, Ref. 14, p. 101):

$$p_b = (1 - Hp_a)p_{b_0} \quad (40)$$

But by Assumption 7,

$$p = p_a + p_b \quad (41)$$

Combining Eqs. (40) and (41) and solving for  $p_a$  yields

$$p_a = \frac{p - p_{b_0}}{1 - Hp_{b_0}} \quad (42)$$

By Assumption 7, the mass flow rate of each component in the gas phase can be written

$$\dot{m}_{a_g} = \frac{W_{a_g} p_a}{RT_g} \dot{v}_g \quad (43)$$

$$\dot{m}_{b_g} = \frac{W_{b_g} p_b}{RT_g} \dot{v}_g \quad (44)$$

where  $W_{a_g}$  and  $W_{b_g}$  are the effective molecular weights of gaseous A and B, respectively, and  $\dot{v}_g$  is the gas volume flow rate.

The gas flow rate from Eq. (13) is

$$\dot{m}_g = \frac{W_g p}{RT_g} \dot{v}_g \quad (45)$$

Adding  $\dot{m}_{a_g}$  and  $\dot{m}_{b_g}$  and equating to  $\dot{m}_g$  yields

$$W_g = \frac{W_{a_g} p_a + W_{b_g} p_b}{p} \quad (46)$$

Substituting  $\dot{v}_g$  from Eq. (45) then gives expressions for  $\dot{m}_{a_g}$  and  $\dot{m}_{b_g}$  in terms of molecular weights and pressures:

$$\dot{m}_{a_g} = \dot{m}_g \frac{W_{a_g} p_a}{W_g p} \quad (47)$$

$$\dot{m}_{b_g} = \dot{m}_g \frac{W_{b_g} p_b}{W_g p} \quad (48)$$

From Eq. (48), the value of  $\beta = \dot{m}_{b_g}/\dot{m}_g$ , the fraction of B vapor in the gas, is

$$\beta = \frac{W_{b_g} p_b}{W_g p} \quad (49)$$

The mass ratio of component B to component A,  $r_c = \dot{m}_b/\dot{m}_a$ , can be written

$$r_c = \frac{\dot{m}_{b_l} + \dot{m}_{b_g}}{\dot{m}_{a_l} + \dot{m}_{a_g}} = \frac{\dot{m}_l - \dot{m}_{a_l} + \dot{m}_{b_g}}{\dot{m}_g - \dot{m}_{b_g} + \dot{m}_{a_l}} \quad (50)$$

Solving Eq. (50) for  $r = \dot{m}_l/\dot{m}_g$  and employing the definitions of  $\alpha$  and  $\beta$ , the mass ratio of liquid to gas is

$$r = \frac{r_c - (1 + r_c)\beta}{1 - (1 + r_c)\alpha} \quad (51)$$

By Assumption 10, the volume flow rate of each component in the liquid is

$$\dot{v}_{a_l} = \frac{\dot{m}_{a_l}}{\rho_{a_l}} \quad (52)$$

and

$$\dot{v}_{b_l} = \frac{\dot{m}_{b_l}}{\rho_{b_l}} = \frac{\dot{m}_l - \dot{m}_{a_l}}{\rho_{b_l}} \quad (53)$$

where  $\rho_{a_l}$  and  $\rho_{b_l}$  are the densities of liquid A and B, respectively.

From Eqs. (52) and (53) and the definition of  $\alpha$ , the liquid density is

$$\rho_l = \frac{1}{(\alpha/\rho_{a_l}) + (1 - \alpha)/\rho_{b_l}} \quad (54)$$

The specific heats of the phases are the mass-weighted averages (Ref. 15, p. 494).

$$c_g = (1 - \beta) c_{a_g} + \beta c_{b_g} \quad (55)$$

$$c_l = \alpha c_{a_l} + (1 - \alpha) c_{b_l} \quad (56)$$

The liquid viscosity is taken as the mass-weighted average:

$$\mu_l = \alpha \mu_{a_l} + (1 - \alpha) \mu_{b_l} \quad (57)$$

The relation adopted for the viscosity of the gas mixture is Wilke's equation (Ref. 15, p. 494):

$$\mu_g = \frac{\mu_{a_g}}{1 + (X_b/X_a) \phi_{ab}} + \frac{\mu_{b_g}}{1 + (X_a/X_b) \phi_{ba}} \quad (58)$$

where  $X_b/X_a$  is the mole ratio given by

$$\frac{X_b}{X_a} = \left( \frac{\beta}{1 - \beta} \right) \frac{W_{a_g}}{W_{b_g}} \quad (59)$$

and  $\phi_{ij}$  is given by

$$\phi_{ij} = \frac{[1 + (\mu_{i_g}/\mu_{j_g})^{1/2} (W_{j_g}/W_{i_g})^{1/4}]^2}{2\sqrt{2} [1 + W_{i_g}/W_{j_g}]^{1/2}} \quad (60)$$

The relation adopted for the thermal conductivity of the gas mixture is the Lindsay and Bromley relation (Ref. 15, p. 494):

$$k_g = \frac{k_{a_g}}{1 + (X_b/X_a) B_a} + \frac{k_{b_g}}{1 + (X_a/X_b) B_b} \quad (61)$$

where

$$B_a = \frac{1}{4} \left\{ \left[ 1 + \frac{\mu_{a_g}}{\mu_{b_g}} \left( \frac{W_{b_g}}{W_{a_g}} \right)^{3/4} \left( \frac{1 + S_a/T_g}{1 + S_b/T_g} \right) \right]^{1/2} \right\}^2 \times \frac{1 + \sqrt{S_a S_b/T_g}}{1 + S_a/T_g} \quad (62)$$

and

$$B_b = \frac{1}{4} \left\{ \left[ 1 + \frac{\mu_{b_g}}{\mu_{a_g}} \left( \frac{W_{a_g}}{W_{b_g}} \right)^{3/4} \left( \frac{1 + S_b/T_g}{1 + S_a/T_g} \right) \right]^{1/2} \right\}^2 \times \frac{1 + \sqrt{S_a S_b/T_g}}{1 + S_b/T_g} \quad (63)$$

The quantities  $S_a$  and  $S_b$  are the Sutherland constants for the components, and may be roughly approximated by  $1.5 T_b$ , where  $T_b$  is the normal boiling temperature.

*g. Coefficients.* The Reynolds number of the slip flow between the gas and a drop is

$$Re = \frac{\rho_g D \bar{V} |s|}{\mu_g} \quad (64)$$

The relationships employed for computing the drop drag coefficient  $C_D$  from  $Re$  are plotted in Fig. 2. For Reynolds numbers less than 0.1, the drag coefficient is given by Stokes Law:

$$C_D = \frac{24}{Re} \quad Re \leq 0.1 \quad (65)$$

For  $0.1 < Re < 2 \times 10^4$ , the  $C_D$  data for solid spheres are represented by Stonecypher's least-squares fit (Ref. 16, p. 3) to Perry's tabulation (Ref. 17, p. 5-61):

$$\log_e C_D = 3.271 - 0.8893 (\log_e Re) + 0.03417 (\log_e Re)^2 + 0.001443 (\log_e Re)^3 \quad 0.1 < Re \leq 2 \times 10^4 \quad (66)$$

For Reynolds numbers greater than  $2 \times 10^4$ ,  $C_D$  is taken as constant at 0.4569, the Eq. (66) value for  $Re = 2 \times 10^4$ .

The  $C_D$  values for solid spheres are only a rough approximation to the values that can be encountered with liquid drops, because the drops can deform into other shapes. The data bands for three sets of drop experiments are included in Fig. 2. Ingebo (Ref. 18) measured drag coefficients for drops of 0.001- to 0.005-in. diameter rapidly accelerating in air streams; at the highest Reynolds numbers of the experiments, the  $C_D$  values were only a third of the solid-sphere values. Hughes and Gilliland (Ref. 19) surveyed the information on drops falling in air and found that the drag coefficient became higher than the solid sphere values at Reynolds numbers above about 200. Rabin, Schallennmuller, and Lawhead (Ref. 20) observed the acceleration of fuel drops in a shock tube and found  $C_D$  values as high as 2.0 at a Reynolds number of  $10^4$ , where the solid sphere value is 0.5. The Reynolds numbers for the two-phase nozzles discussed in this report were all in the range of 100 to 4000, with the higher values at the inlet and the lower values at the exit of the nozzles.

Thus, there are two factors which are expected to make the drag on the liquid phase larger in practice than assumed in this analysis. First, the drop size in practice will have the Weber number = 6 value as the upper



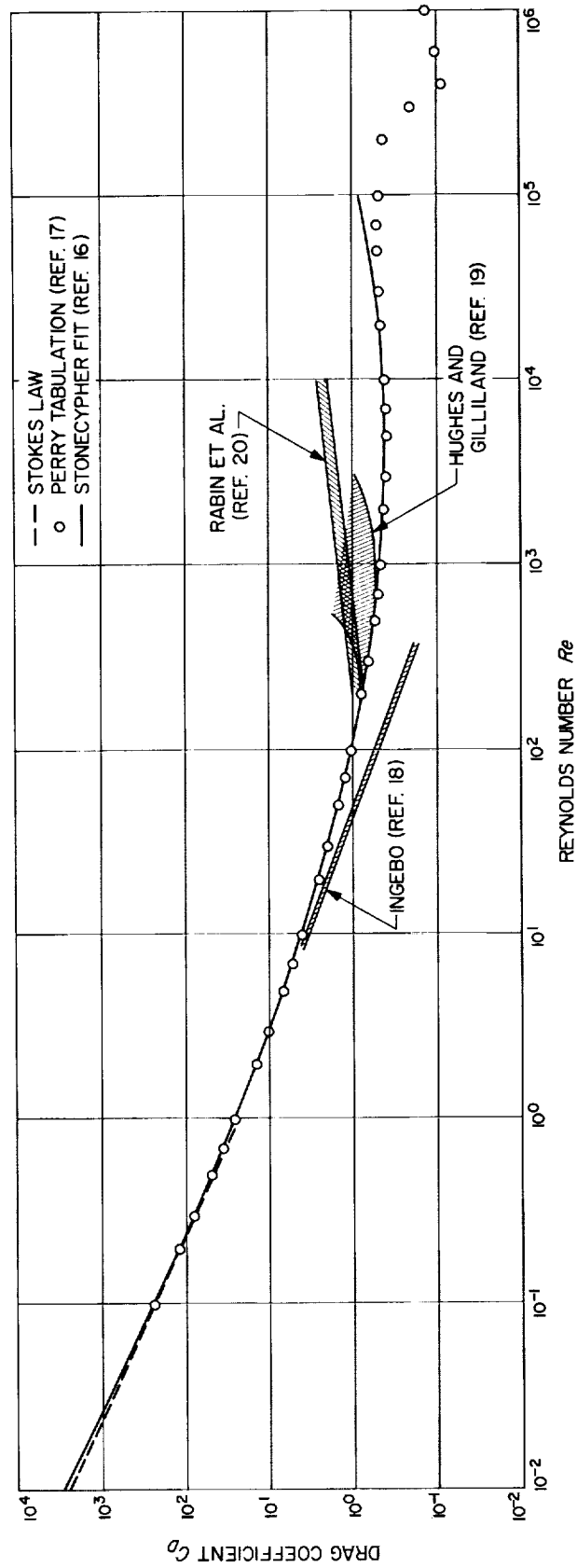


Fig. 2. Drag coefficient of spheres and drops

limit, whereas the analysis employs that value for the mean size. Second, the drag coefficient in practice, at least at the higher Reynolds numbers, is larger than the solid-sphere coefficient assumed in the analysis.

From Ref. 21 (pp. 414-415), the drop heat-transfer coefficient is taken as

$$h = \frac{2k_g}{D} \quad Re \leq 1.0 \quad (67)$$

$$h = c_g \rho_g \bar{V} |s| \left( \frac{2.2}{Re} + \frac{0.48}{\sqrt{Re}} \right) \quad 1.0 < Re \leq 25 \quad (68)$$

$$h = \frac{0.37 k_g Re^{0.8}}{D} \quad Re > 25 \quad (69)$$

These equations complete the analysis of frictionless two-component flow with a prescribed pressure profile  $p(x)$ .

**3. Optimum pressure profile.** The optimum pressure profile is the one that maximizes the mean exit velocity (which is also the velocity attained by the liquid after exhausting into a constant-pressure region) for a given nozzle length  $L$ . That is, it is desired that  $\bar{V}_e$ , or, for greater mathematical convenience,  $\bar{V}_e^2$ , meet the requirement

$$\bar{V}_e^2 = \bar{V}_0^2 + \int_{p_0}^{p_e} \frac{d\bar{V}^2}{dp} dp = \text{maximum} \quad (70)$$

subject to the constraint that

$$x_e = \int_{p_0}^{p_e} \frac{dx}{dp} dp = \text{fixed} \quad (71)$$

Since the equations of the preceding section can be solved by specifying the slip  $s$  directly as the independent variable instead of calculating  $s$  from the pressure profile through Eq. (28), the integrand of Eq. (70) can be considered a function of  $s$  and  $p$ ; namely, from Eq. (14),

$$\frac{d\bar{V}^2}{dp} = -\frac{2}{1+r} \left( \frac{1}{a\rho_g} + \frac{r}{b\rho_l} \right) = F(s, p) \quad (72)$$

From Eq. (29), the integrand of Eq. (71) is

$$\begin{aligned} \frac{dx}{dp} = & \frac{4D}{3\rho_g |s| s C_D \bar{V}^2} \left[ 1 + \frac{b^2 \rho_l}{2} \frac{d\bar{V}^2}{dp} \right. \\ & \left. + \frac{b\rho_l \bar{V}^2}{1+r} \left( \frac{s}{1+r} \frac{dr}{dp} - \frac{ds}{dp} \right) \right] \end{aligned} \quad (73)$$

Numerical estimates show that  $dr/dp$  and  $ds/dp$  are small enough in a two-phase nozzle so that the last term in Eq. (73) can be neglected. Hence,  $dx/dp$  is approximately

$$\frac{dx}{dp} = \frac{4D}{3\rho_g |s| s C_D \bar{V}^2} \left( 1 + \frac{b^2 \rho_l F(s, p)}{2} \right) = G(s, p) \quad (74)$$

Thus, the problem is to find the function  $s(p)$  for which

$$\int_{p_0}^{p_e} F(s, p) dp = \text{maximum} \quad (75)$$

subject to the constraint that

$$\int_{p_0}^{p_e} G(s, p) dp = \text{fixed} \quad (76)$$

This is the isoperimetric problem of the calculus of variations. The desired maximizing function, designated  $s_0(p)$ , is found (Ref. 22, pp. 216-218) by forming the function

$$F^* = F - \lambda G \quad (77)$$

and solving

$$\frac{\partial F^*}{\partial s} = 0 \quad (78)$$

where  $\lambda$  is a constant, the Lagrangian multiplier, which has the units of acceleration here. It is a constant which specifies the length of the nozzle for given fluid properties and inlet conditions; the method of selecting it will be discussed in Section IV.

Substituting Eqs. (74) and (77) into Eq. (78), the optimum slip is the solution of

$$\frac{\partial F}{\partial s} - \frac{4D\lambda}{3\rho_g \bar{V}^2} \frac{\partial}{\partial s} \left[ \frac{1}{|s| s C_D} \left( 1 + \frac{b^2 \rho_l F}{2} \right) \right] = 0 \quad (79)$$

Combining the terms in  $\partial F/\partial s$ , this becomes

$$\begin{aligned} \left( 1 - \frac{2D\lambda b^2 \rho_l}{3\rho_g \bar{V}^2 |s| s C_D} \right) \frac{\partial F}{\partial s} - \frac{2D\lambda \rho_l F}{3\rho_g \bar{V}^2 |s| s C_D} \frac{\partial b^2}{\partial s} \\ - \frac{4D\lambda}{3\rho_g \bar{V}^2} \left( 1 + \frac{b^2 \rho_l F}{2} \right) \frac{\partial}{\partial s} \left( \frac{1}{|s| s C_D} \right) = 0 \end{aligned} \quad (80)$$

Evaluating  $F$  from Eq. (72), performing the indicated differentiations, and solving for  $s$ , the relation for the optimum slip (for frictionless flow) is

$$s_o = - \frac{\Delta p c^{1/2}}{|\Delta p|} \left( \frac{fg s_o + e C'_d}{2g(d-1)} \right)^{1/2} \quad (81)$$

where

$$c = \frac{4D\lambda b^2 \rho_l}{3\rho_g \bar{V}^2 C_d} \quad (82)$$

$$d = \frac{b^2 \rho_l}{a^2 \rho_g} \quad (83)$$

$$e = \frac{b^2 \rho_l}{a\rho_g(1+r)} + \frac{br}{1+r} - 1 \quad (84)$$

$$f = d \left( \frac{2a}{br} + 1 \right) + 1 \quad (85)$$

$$g = \frac{r}{(1+r)^2} \quad (86)$$

and

$$C'_d = 1.0 \quad Re \leq 0.1611 \quad (87)$$

$$C'_d = 1.1107 + 0.06854 \log_e Re + 0.004329 (\log_e Re)^2 \quad (88)$$

$$0.1611 < Re \leq 4.709 \times 10^3$$

$$C'_d = 2.0 \quad Re > 4.709 \times 10^3 \quad (89)$$

A similar analysis was employed by Marble (Ref. 23) to find the optimum nozzle shape with Stokes flow.

In the computer programs the  $(d-1)$  term in Eq. (81) is replaced by  $d$ , with negligible error at the small slip values of a high-performance nozzle; the substitution avoids numerical difficulties in calculating  $s_o$  for the initial pressure step in some nozzles, where the slip could initially be high enough to give  $d=1$ , and the results should be considered invalid in any part of a nozzle where  $d$  is less than about 5.

Equation (81) can be simplified to give a rule for finding the optimum nozzle contour for many cases of practical interest. If  $r$  and  $\rho_l/\rho_g$  are large,  $s_o$  is small, and  $Re$  does not vary greatly, the quantity in parentheses in Eq. (81) is nearly constant. If  $D$  is constant and the flow

is nearly isothermal, so that  $\rho_g$  is proportional to the pressure  $p$ , then Eq. (81) reduces to

$$s_o = \text{const} \times \left( \frac{1}{p\bar{V}^2} \right)^{1/2} \quad (90)$$

To utilize Eq. (90), the  $V(p)$  relationship for isentropic flow can be substituted to give the optimum slip  $s_o$  as a function of pressure for a given initial slip. The optimum slip can then be substituted in Eq. (74) to give the optimum  $dx/dp$  from which  $x(p)$  can be calculated. The nozzle length is determined by the initial slip assumed.

**4. Wall shear and boundary layer.** The momentum thickness  $\theta$  of a boundary layer is the thickness of free-stream flow which has a momentum flux equal to that by which the momentum flux of frictionless nozzle flow exceeds the momentum flux of the real flow for the same mass flux (Ref. 24, p. 5). For a two-phase nozzle, the momentum flux of the frictionless nozzle flow is that given by Eq. (7):

$$\dot{M} = \dot{m}_t \bar{V} \quad (91)$$

The mean mixture density corresponding to the mean velocity  $\bar{V}$  is

$$\rho' = \frac{\dot{m}_t}{A\bar{V}} = \frac{\rho_l}{1+r_a} \quad (92)$$

where  $r_a$  is the ratio of gas flow area to liquid flow area  $\rho_l V_l / r \rho_g V_g$ .

From the definition of the momentum thickness, the value of  $\theta$  at a station where the nozzle wall radius is  $y_o$  is given by

$$\dot{M} - \dot{M}_f = 2\pi y_o \theta \frac{\dot{m}_t \bar{V}}{A} = 2\pi y_o \rho' \bar{V}^2 \theta \quad (93)$$

where  $\dot{M}_f$  is the momentum flux of the real flow with friction.

Equation (93) is identical to the definition of  $\theta$  for single-phase flow (Ref. 24, Eq. 11), with the single phase  $\rho$  replaced by  $\rho'$  and the single-phase  $V$  replaced by  $\bar{V}$ . The skin-friction coefficient can be defined using the same quantities.

$$C_f = \frac{2\tau_w}{\rho' \bar{V}^2} \quad (94)$$

where  $\tau_w$  is the wall shear. It will be shown that a valid  $C_f$  value can be provided.

The boundary-layer momentum equation (Ref. 24, Eq. 22) then becomes

$$d\theta = \frac{C_f}{2} dx - \theta \left[ \frac{1 + (\delta^*/\theta)}{\bar{V}} d\bar{V} + \frac{1}{\rho'\bar{V}} d(\rho'\bar{V}) + \frac{1}{R_w} dR_w \right] \quad (95)$$

where  $\delta^*$  is the displacement thickness, i.e., the distance the wall must be moved outward to give the same flow rate as with frictionless flow.

Assuming a  $1/2$ -power velocity profile and no density variation ( $\rho' = \text{const}$  and  $\delta_r' = \delta$  in Ref. 24), the shape factor  $\delta^*/\theta$  is obtained from Eqs. (9) and (12) of Ref. 24.

$$\frac{\delta^*}{\theta} = \frac{\int_0^\delta [1 - (y/\delta)^{1/2}] dy}{\int_0^\delta (y/\delta)^{1/2} [1 - (y/\delta)^{1/2}] dy} = \frac{9}{7} \quad (96)$$

where  $\delta$  is the velocity thickness of the boundary layer.

Noting that  $d\bar{V}$  can be written  $d\bar{V}^2/2\bar{V}$ , and that  $d(\rho'\bar{V}) = d(\dot{m}_t/A)$  from Eq. (92), the finite-difference form of Eq. (95) is

$$\Delta\theta = \frac{C_{f_m}}{2} \Delta x - \theta_m \left( \frac{8}{7\bar{V}_m^2} \Delta\bar{V}^2 - \frac{1}{A_m} \Delta A + \frac{1}{y_{o_m}} \Delta y_o \right) \quad (97)$$

Wall shear in homogeneous two-phase flow has been found (Ref. 25, p. 181) to be equal to that which would exist with pure liquid at equal velocity and boundary-layer thickness, multiplied by the wetted wall fraction:

$$\tau_w = \frac{C_{f_l}}{2} \rho_l V_l^2 \frac{A_l}{A} = \frac{C_{f_l} \rho_l V_l^2}{2(1 + r_a)} \quad (98)$$

where  $C_{f_l}$  is the skin friction coefficient for liquid at a Reynolds number of

$$R_\delta = \frac{\rho_l V_l \delta}{\mu_l} \quad (99)$$

For a  $1/2$ -power profile, the velocity thickness, from Eq. (12) of Ref. 24, is

$$\delta = \frac{72}{7} \theta \quad (100)$$

A convenient relation for  $C_{f_l}$  as a function of  $R_\delta$  is the Shultz-Grunow relation (Ref. 15, p. 147) which, with the aid of Eq. (6-35) of Ref. 15, can be written

$$C_{f_l} = \frac{0.208}{(\log_{10} R_\delta + 0.425)^{2.584}} \quad (101)$$

Comparison of Eqs. (94) and (98) shows that  $C_f$  can be written

$$C_f = \frac{rb}{1+r} C_{f_l} \quad (102)$$

Thus, the final form of the boundary-layer momentum equation is

$$\Delta\theta = \frac{r_m b_m}{1+r_m} C_{f_l} \Delta x - \theta_m \left( \frac{8\Delta\bar{V}^2}{7\bar{V}_m^2} - \frac{\Delta A}{A_m} + \frac{\Delta y_o}{y_{o_m}} \right) \quad (103)$$

Let  $\bar{V}_\delta$  be the mean velocity of the flow including the boundary layer. Then, from Eq. (93),

$$\dot{m}_t \bar{V}_\delta = \dot{M}_f = \dot{m}_t \bar{V} - 2\pi y_o \rho' \bar{V}^2 \theta \quad (104)$$

Hence, employing Eq. (92), the mean exit velocity including the boundary layer is

$$\bar{V}_\delta = \bar{V} \left( 1 - \frac{2\pi y_o \theta}{A} \right) \quad (105)$$

By the definition of the displacement thickness, the flow rate is reduced by the throat displacement thickness  $\delta_t^*$  to

$$\dot{m}_\delta = \dot{m}_t \left( 1 - \frac{2\delta_t^*}{y_{o_t}} \right) \quad (106)$$

**5. Auxiliary quantities.** The foregoing equations provide a solution for the basic dependent variables of the two-component nozzle flow problem. In this section, expressions will be presented for additional parameters that are useful in nozzle design and cycle studies.

*a. Equilibrium exhaust conditions.* If the nozzle exhausts into a constant pressure region such as the atmosphere or the interior of a separator or condenser, then

the velocities and temperatures of the two phases can reach equality at  $\bar{V}$  and  $\bar{T}$ , respectively. The velocity  $\bar{V}$  is that given by Eq. (6). The equilibrium temperature  $\bar{T}$  is found by applying Eq. (23) to the constant-pressure process:

$$\begin{aligned} \Delta \bar{T}_g = \bar{T} - T_g = & -\frac{1}{\bar{c}_{gm}} \left[ \frac{\Delta \bar{V}_g^2}{2} + \bar{r} \left( \bar{c}_{lm} \Delta \bar{T}_l + \frac{\Delta \bar{V}_l^2}{2} \right) \right. \\ & + \frac{\Delta \bar{m}_g}{\bar{m}_g} \left( \frac{\delta V^2}{2} \right) + \frac{\Delta \bar{m}_{a_g}}{\bar{m}_g} (L_a + c_{a_g} \delta T) \\ & \left. + \frac{\Delta \bar{m}_{b_g}}{\bar{m}_g} (L_b + c_{b_g} \delta T) \right] \end{aligned} \quad (107)$$

where unsubscripted quantities are those at the exit, barred quantities are those after equilibrium is reached, barred  $\Delta$ 's are changes between the two, and sub  $m$ 's designate quantities evaluated at the mean temperature between the two.

Solving for  $\Delta \bar{T}_l$ ,

$$\begin{aligned} \Delta \bar{T}_l = & -\frac{1}{\bar{r} \bar{c}_{lm}} \left[ \bar{c}_{gm} \Delta \bar{T}_g + \frac{\Delta \bar{V}_g^2}{2} + \bar{r} \frac{\Delta \bar{V}_l^2}{2} \right. \\ & + \frac{\Delta \bar{m}_{a_g}}{\bar{m}_g} (L_a + c_{a_g} \delta T) + \frac{\Delta \bar{m}_{b_g}}{\bar{m}_g} (L_b + c_{b_g} \delta T) \\ & \left. + \frac{\Delta \bar{m}_g}{\bar{m}_g} \left( \frac{\delta V^2}{2} \right) \right] \end{aligned} \quad (108)$$

Setting  $T = \bar{T}$  and  $V_g = V_l = \bar{V}$  in the phase property and other relations yields the remaining equilibrium exhaust conditions.

*b. Nozzle geometry.* For a circular nozzle (Fig. 1) the radius  $y_o$  is given by

$$y_o = \sqrt{\frac{A}{\pi}} \quad (109)$$

The wall angle  $\omega_o$  is given by

$$\tan \omega_o = \frac{\Delta y_o}{\Delta x} \quad (110)$$

The geometry for an annular nozzle is shown in Fig. 3. The inboard half-area is given by

$$\frac{A}{2} = \frac{\pi (R_\phi^2 - R_i^2)}{\cos \phi} \quad (111)$$

The outboard half-area is given by

$$\frac{A}{2} = \frac{\pi (R_o^2 - R_\phi^2)}{\cos \phi} \quad (112)$$

The radius from the axis to the flow centerline is

$$R_\phi = R_{\phi_0} - x \sin \phi \quad (113)$$

Solving Eqs. (111) and (112) for  $R_i$  and  $R_o$  yields

$$R_i = \sqrt{R_\phi^2 - \frac{A \cos \phi}{2\pi}} \quad (114)$$

and

$$R_o = \sqrt{R_\phi^2 + \frac{A \cos \phi}{2\pi}} \quad (115)$$

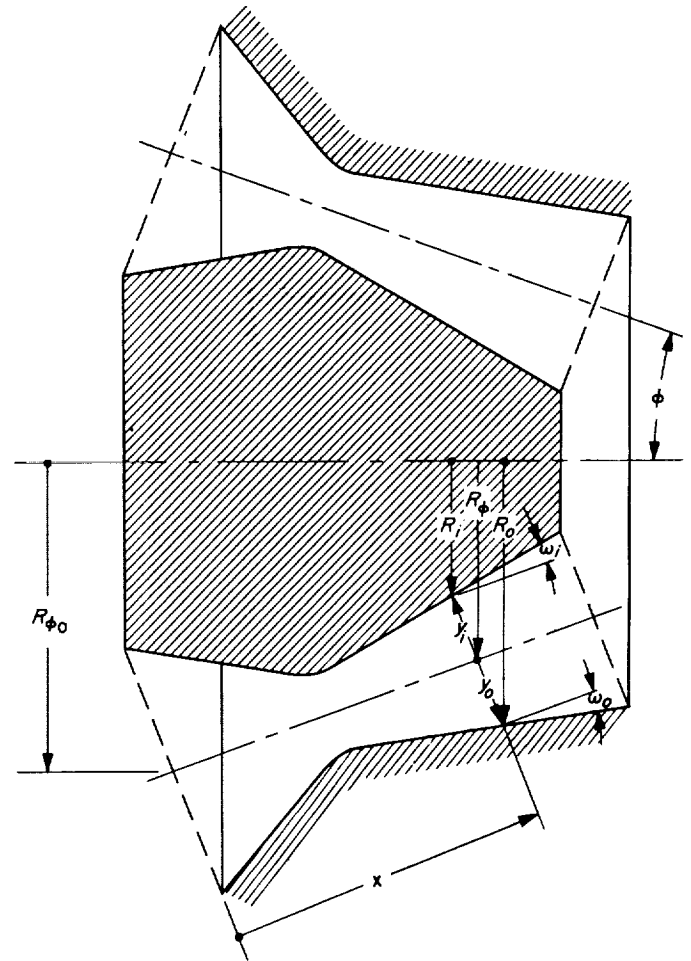


Fig. 3. Annular nozzle geometry

The wall coordinates are

$$y_i = \frac{R_\phi - R_i}{\cos \phi} \quad (116)$$

and

$$y_o = \frac{R_o - R_\phi}{\cos \phi} \quad (117)$$

The wall angles are

$$\tan \omega_i = \frac{\Delta y_i}{\Delta x} \quad (118)$$

and

$$\tan \omega_o = \frac{\Delta y_o}{\Delta x} \quad (119)$$

The annular geometry can be employed in studying rectangular nozzles by selecting a large value of  $R_\phi$  and a flow rate that gives the desired nozzle height  $y_o + y_i$ .

*c. Impingement parameters.* For convenience in determining the velocity reduction of the liquid due to impingement on the wall of a separator or condenser, two quantities required in the separator analysis of Ref. 26 are computed.

Assuming that impingement takes place on a cone of base area equal to the equilibrium jet area  $\bar{A}$ , the

**Table 1. Conversion factors employed in computer programs<sup>a</sup>**

Equation number	Multiply	By
1	Right side	0.02645
2, 133	Right side	144
17, 134	Right side	4633.04
23, 108, 130 } 132, 136, 137 }	{ $V^2$ terms	25,036.47 <sup>-1</sup>
28, 29	$\Delta p$	5.4039 <sup>-1</sup>
37	$\Delta p$	4633.04
64	$h_m$	3600 <sup>-1</sup>
67, 69	Right side	300
68	Right side	12
82	Right side	3600
98	Right side	12 <sup>-1</sup>
122	Right side	4633.04 <sup>-1</sup>
123	Right side	43,200
	Right side	144 <sup>-1</sup>

<sup>a</sup> Based on 32.1739 lbm-ft/lbf-s<sup>2</sup>, 778.161 ft-lbf/Btu, 0.03281 ft/cm, 2.248 × 10<sup>-6</sup> lbf/dyn.

Reynolds number of the liquid film at the mid-area of the cone will be

$$Re_f = \frac{\bar{\rho}_l V t_f}{\bar{\mu}_l} \quad (120)$$

where  $V$  is the film velocity and  $t_f$  is the collected film thickness at circumference  $(2\pi\bar{A})^{1/2}$ . For zero void fraction of the film,  $V$  is given by

$$\frac{\bar{m}_l}{2} = \bar{\rho}_l \bar{V} t_f (2\pi\bar{A})^{1/2} \quad (121)$$

Hence, the mean film Reynolds number is

$$Re_f = \frac{\bar{m}_l}{\bar{\mu}_l (8\pi\bar{A})^{1/2}} \quad (122)$$

The liquid velocity reduction depends on the ratio of the mass flux for all-liquid flow to the actual mass flux. This ratio is

$$Q = \frac{\bar{\rho}_l \bar{V} \bar{A}}{\bar{m}_l} \quad (123)$$

which is  $2/C_f$  times the  $Q$  defined in Ref. 26.

**6. Units.** The units employed for each quantity are listed in the Nomenclature. Computer input and output quantities are in those units. Those equations requiring conversion factors, and the values of the factors, are listed in Table 1.

## B. One-Component Flow

**1. Assumptions.** Assumptions 1-6 of the two-component analysis are retained. The additional assumption is made that both phases are at the saturation temperature corresponding to the local pressure. This is realistic in that evaporation of the liquid and condensation of the vapor strongly drive the temperatures of both phases toward the saturation value.

### 2. Derivation of equations for free-stream flow

*a. Continuity.* Equation (2) is still valid for this case. One notation change is made, however. The mixture quality  $X_g = \dot{m}_g/\dot{m}_t$  is employed in place of the mixture

ratio  $r = \dot{m}_l/\dot{m}_g$  throughout the one-component program, and  $r$  is everywhere replaced by

$$r = \frac{1}{\lambda_g} \frac{X_g}{X_l} \quad (124)$$

and changes in  $r$  by

$$\Delta r = - \frac{\Delta X_g}{X_l} \quad (125)$$

*b. Momentum.* Equation (17) is valid for this case except that, in accordance with the equal-temperature assumption,  $T_{g_m}$  is simply the mid-interval saturation temperature  $T_m$ .

*c. Energy.* The total enthalpy of the vapor phase is

$$H_g = \dot{m}_g \left( h_g + \frac{V_g^2}{2} \right) \quad (126)$$

where  $h_g$  is the saturated vapor enthalpy, and the total enthalpy of the liquid phase is

$$H_l = \dot{m}_l \left( c_l T + \frac{p}{\rho_l} + \frac{V_l^2}{2} \right) \quad (127)$$

The energy equation for the mixture is

$$\Delta \left[ \dot{m}_g \left( h_g + \frac{V_g^2}{2} \right) + \dot{m}_l \left( c_l T + \frac{p}{\rho_l} + \frac{V_l^2}{2} \right) \right] = 0 \quad (128)$$

or

$$\begin{aligned} \Delta \dot{m}_g \left( h_{g_m} + \frac{V_{g_m}^2}{2} \right) + \dot{m}_{g_m} \left( \Delta h_g + \frac{\Delta V_g^2}{2} \right) \\ + \Delta \dot{m}_l \left( c_{l_m} T + \frac{p_m}{\rho_{l_m}} + \frac{V_{l_m}^2}{2} \right) \\ + \dot{m}_{l_m} \left( c_{l_m} \Delta T + \frac{\Delta p}{\rho_{l_m}} + \frac{\Delta V_l^2}{2} \right) = 0 \end{aligned} \quad (129)$$

Dividing by  $\dot{m}_l$  and rearranging gives the quality change across the pressure increment.

$$\begin{aligned} \Delta X_g = - \frac{1}{L_m + \frac{V_{g_m}^2 - V_{l_m}^2}{2}} \left[ X_{g_m} \left( \Delta h_g + \frac{\Delta V_g^2}{2} \right) \right. \\ \left. + (1 - X_{g_m}) \left( c_{l_m} \Delta T + \frac{\Delta p}{\rho_{l_m}} + \frac{\Delta V_l^2}{2} \right) \right] \end{aligned} \quad (130)$$

*d. Drag.* Equations (28) and (29) correctly express the drag relation for this case.

*e. Heat transfer.* Heat-transfer considerations are eliminated by the assumption of equal temperatures for the two phases. The one-component case reduces to four equations (1, 17, 28, and 130) in the four unknowns,  $D$ ,  $V_g$ ,  $V_l$ , and  $X_g$ .

*3. Optimum pressure profile.* Equation (81) is valid for the one-component, as well as the two-component, case.

*4. Wall shear and boundary layer.* Again, the equations are the same as for the two-component case.

*5. Auxiliary quantities.* The energy equation for attainment of equilibrium at constant pressure is

$$\dot{m}_g \left( h_g + \frac{V_g^2}{2} \right) + \dot{m}_l \left( h_l + \frac{V_l^2}{2} \right) = \dot{m}_t \bar{V}^2 + \bar{m}_g \bar{h}_g + \bar{m}_l \bar{h}_l \quad (131)$$

Dividing by  $\dot{m}_l$ , setting  $h_l = \bar{h}_l$ , and rearranging gives

$$\bar{X}_g = X_g \left( 1 + \frac{V_g^2}{2L} \right) + (1 - X_g) \frac{V_l^2}{2L} - \frac{\bar{V}^2}{2L} \quad (132)$$

*6. Units.* The conversion factors for the one-component equations are listed with the two-component factors in Table 1.

## C. Isentropic Flow

In the limit as drop size approaches zero, the phase temperatures and velocities approach equality and the nozzle flow becomes a reversible, isentropic process. The corresponding exit velocity is the maximum attainable for any given inlet conditions.

### 1. Two-component flow

*a. Continuity.* With  $V_g = V_l$ , Eq. (2) reduces to

$$A = \frac{\dot{m}_g}{V} \left( \frac{1}{\rho_g} + \frac{r}{\rho_l} \right) \quad (133)$$

*b. Momentum.* With  $s = 0$ , Eq. (17) reduces to

$$\Delta V^2 = - \frac{2}{1 + r_m} \left( \frac{RT_m}{W_{g_m}} \log_e \frac{p + \Delta p/2}{p - \Delta p/2} + \frac{r_m \Delta p}{\rho_{l_m}} \right) \quad (134)$$

c. *Energy*. With  $V_g = V_l$  and  $T_g = T_l$ , Eq. (23) reduces to

$$\Delta T = -\frac{1}{c_{gm}} \left[ \frac{\Delta V^2}{2} + r_2 \left( c_{lm} \Delta T + \frac{\Delta p}{\rho_{lm}} + \frac{\Delta V^2}{2} \right) + \frac{\Delta \dot{m}_{ag}}{\dot{m}_{g2}} L_{a1} + \frac{\Delta \dot{m}_{bg}}{\dot{m}_{g2}} L_{b1} \right] \quad (135)$$

Collecting terms in  $\Delta T$ , this becomes

$$\Delta T = -\frac{1}{c_{gm} + r_2 c_{lm}} \left[ (1 + r_2) \frac{\Delta V^2}{2} + \frac{r_2 \Delta p}{\rho_{lm}} + \frac{L_{a1} \Delta \dot{m}_{ag} + L_{b1} \Delta \dot{m}_{bg}}{\dot{m}_{g2}} \right] \quad (136)$$

## 2. One-component flow

a. *Continuity*. Equation (133) applies to this case.

b. *Momentum*. Equation (134) applies.

c. *Energy*. With  $V_g = V_l$ , Eq. (130) reduces to

$$\Delta X_g = -\frac{1}{L_m} \left[ X_{gm} \left( \Delta h_g + \frac{\Delta V^2}{2} \right) + (1 - X_{gm}) \left( c_{lm} \Delta T + \frac{\Delta p}{\rho_{lm}} + \frac{\Delta V^2}{2} \right) \right] \quad (137)$$

## III. Computer Programs

Computer programs were written for (1) isentropic two-component flow, (2) real two-component flow, (3) isentropic one-component flow, and (4) real one-component flow. ("Real flow" refers to flow with slip.) The real flow programs compute both the frictionless free-stream flow and the friction loss due to the boundary layer. The prescribed quantities are the pressure, drop diameter, and phase velocities and temperatures at the nozzle entrance; the exit pressure; the number of pressure steps desired (for balancing accuracy against computing time); and the fluid properties as a function of temperature or pressure, or both.

Two options are available for the real-flow programs; in the MOP = 0 option, the variation of pressure with distance is specified; in the MOP = 1 option, the pressure variation is optimized. Nozzle geometry and boundary-layer growth can be computed for either a circular nozzle (MGEO = 0) or an annular nozzle (MGEO = 1). In addition, the liquid drops can be assumed to have either a constant diameter (MBU = 0), or to break up to limit the Weber number to 6 (MBU = 1).

The programs begin by storing the tables of fluid properties and computing the nozzle inlet conditions. The programs then proceed half a pressure step at a time. At the middle of each pressure interval, the changes in quantities across the interval are computed using the properties interpolated from the tables for that pressure, and for the existing temperature in the case of those properties tabulated as functions of both  $p$  and  $T$ . The change in slip is found if  $p(x)$  is specified, or a new optimum slip is found if the nozzle is being optimized. At the end of each pressure step, the flow conditions are updated and initial conditions are determined for the next step. The drop size is reduced to  $D_{\max}$  (Eq. 1) at that time if the Weber number exceeds 6 ( $D$  exceeds  $D_{\max}$ ) and the breakup option has been specified. Flow conditions are printed if the pressure is one selected for output. The computations continue until the last pressure step has been completed, and the flow conditions at the smallest flow area encountered are printed as the throat conditions.

## IV. Two-Phase Nozzle Design

The method of utilizing the computer programs to design a two-phase nozzle will now be presented. The design illustrated will be that of the 50-in. nitrogen-water nozzle employed in the experiments described in Section V. The performance results calculated here will also illustrate the characteristics of two-phase nozzles and provide values for comparison with the experimental results.

The flow conditions for which the nozzle is to be designed are: inlet pressure  $p_0 = 150$  psia (typical of inlet pressures for liquid-metal MHD systems); water/nitrogen mass ratio  $r_e = 40$  (typical of MHD systems); inlet temperature  $T_{g0} = T_{l0} = 520^\circ\text{R}$  (mean water temperature in test facility); inlet velocity  $V_{g0} = V_{l0} = 7.3$  ft/s (velocity in the 14-in.-diam inlet of the experimental nozzle); total mass flow rate  $\dot{m}_t = 160$  lbm/s (flow rate calculated for the throat area of the experimental nozzle); and nozzle exit pressure  $p_e = 14.1$  psia (atmospheric pressure at the test facility).

The first step is to determine the optimum nozzle contour using the program option MOP = 1. This option proved useful only for the constant drop diameter option MBU = 0. The optimum pressure gradient at the inlet is so steep that immediate breakup to fine drops is called for by the Weber number = 6 criterion, while the exposure time is too short for that criterion to be valid. Suppression of the breakup until the exposure time reaches the natural period of oscillation of the drops



would have to be added to the programs to permit useful results from simultaneous utilization of the optimization and breakup options, but this would have no practical value because the initial part of the optimum nozzle has an impractically steep wall angle which must be replaced by a more gradual inlet in practice. The optimization option is, therefore, carried out for constant drop diameters which bracket the diameter range encountered in the final design. The range is 0.01 to 0.05 in. (250 to 1250  $\mu\text{m}$ ) for this nozzle.

Computer runs are first made for a series of values of the Lagrangian multiplier  $\lambda$  covering the range of nozzle lengths of possible interest. Figure 4 shows the variation of nozzle length  $L$  (value of  $x$  at  $p = 14.1$  psia) with  $\lambda$  for the two extreme drop diameters. This figure identifies the range  $\lambda = 10^2$ – $10^4$  as encompassing the lengths of possible interest, i.e., 10 to 1000 in. For  $\lambda$  values bracketing the range of interest, say 100 and 3000, the variation of nozzle radius  $y_n$ , normalized by the throat radius  $y_{n,p}$ , is then plotted as a function of fractional distance  $x/L$  through the nozzle, as shown in Fig. 5. The purpose of this plot is to determine whether there is any one contour that satisfactorily fits the optimum contours for the range of lengths and drop diameters being considered. This is seen to be possible, in this instance, where the normalized optimum contours for two widely differing lengths at both of the two drop diameters are closely similar. Any one of the contours can, therefore, be adopted as the basis of a practical nozzle contour.

A preliminary guess must now be made as to the optimum nozzle length to permit modifying the optimum profile into a practical nozzle contour. Too short a nozzle will have a low exit velocity because of large slip, and too long a nozzle will have a low velocity because of large friction. Making the guess that the optimum length corresponds to  $\lambda = 3600$ , the contour for that case, with a 0.01-in. drop diameter, is then plotted as shown by the dashed curve in Fig. 6. This curve has a nearly vertical slope at the inlet. A conical entrance of 20-deg slope is probably the steepest that is practical, and the actual nozzle inlet is, therefore, made a 20-deg line tangent to the optimum contour. The inlet radius, dictated by the injector diameter, was 7 in. for the experimental nozzle. A conical exit is also chosen to replace the flaring exit of the optimum profile, and an angle of 2.5 deg was adopted for the experimental nozzle. The resulting practical nozzle contour is given by the solid lines in Fig. 6. The length of this nozzle is 51.4 in., of which the first 12 in. is only a transition section between the injector and the station where significant acceleration begins.

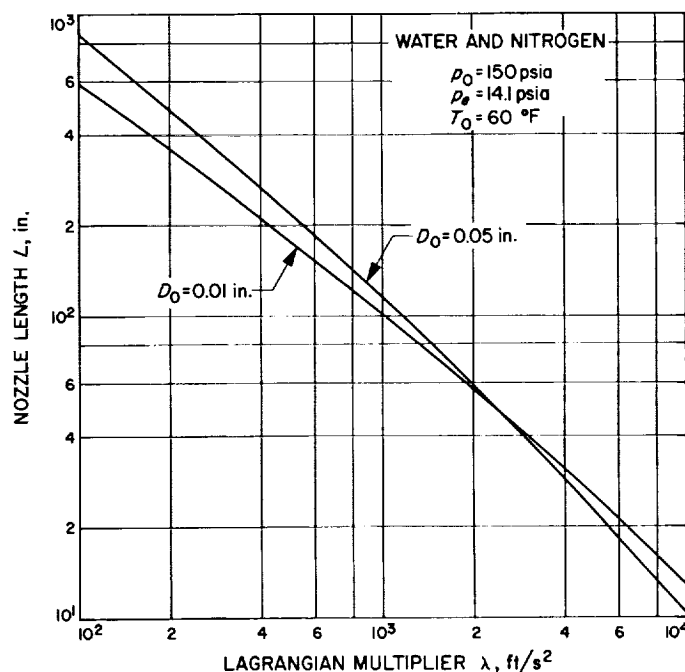


Fig. 4. Correspondence between nozzle length and Lagrangian multiplier

The remainder of the design analysis utilizes the prescribed pressure-versus-distance option  $MOP = 0$ , with the  $p(x)$  profile corresponding to the adopted nozzle contour. From the  $\lambda = 3600$  results, the values of pressure as a function of distance are plotted utilizing the printed  $x$ -values for each pressure in the portion of the optimum nozzle that was retained. For pressures that fall in the conical extensions, the nozzle radius values are read from the computer output, and the corresponding  $x$ -values are calculated for the conical sections. The resulting function  $p(x)$  is plotted in Fig. 7.

The next step is to read off a set of values of  $p$  and  $x$  to make up the  $p(x)$  input table required in the prescribed-pressure option  $MOP = 0$ . The values chosen are shown superimposed on the curve in Fig. 7.

Next, the initial drop diameter for the drop breakup option  $MBU = 1$  must be selected. Figure 8 shows the variation of exit velocity with initial drop diameter for three different nozzle lengths. The 50-in. nozzle employs the  $p(x)$  values from Fig. 7; the other two lengths are obtained by multiplying those  $x$  values by constant factors. The computations show that, with breakup, the exit velocity decreases with increasing initial drop diameter until a diameter is reached above which the velocity is constant. This occurs because any larger drop breaks up to that diameter. If breakup is prevented ( $MBU = 0$ ), the

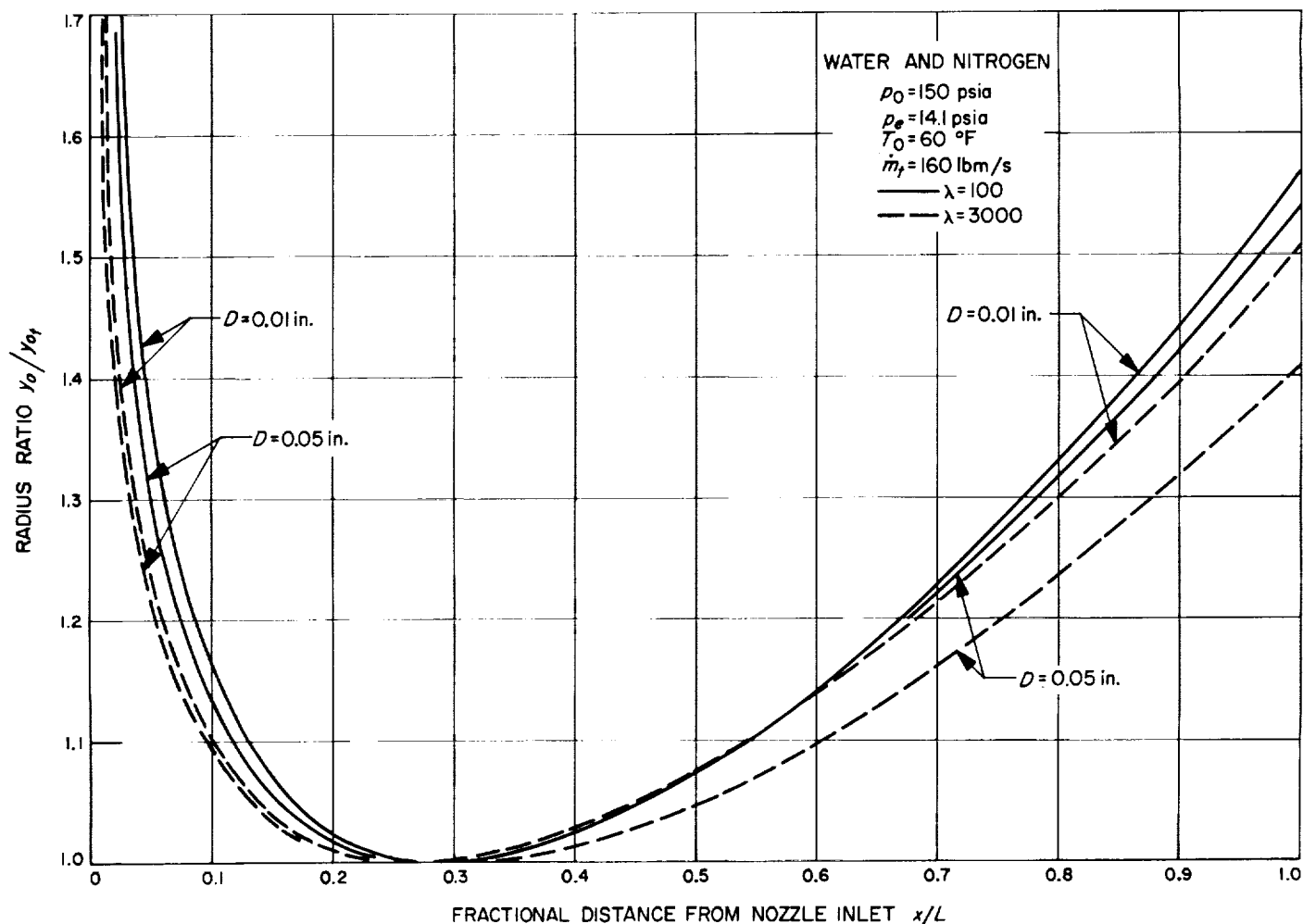


Fig. 5. Normalized profiles of optimum nozzles

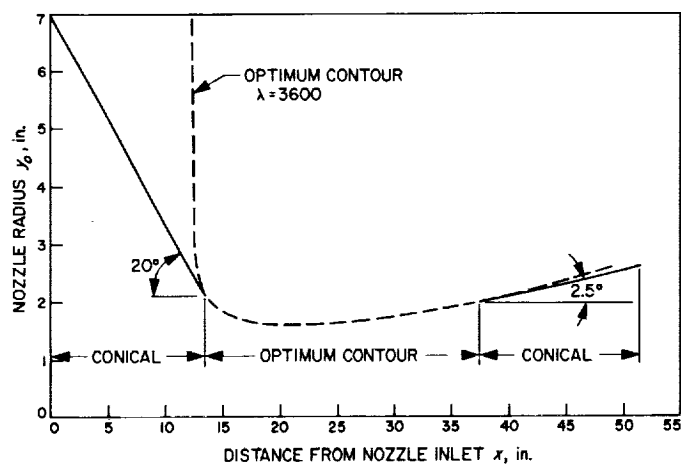


Fig. 6. Modification of optimum shape to obtain experimental nozzle

velocity decreases indefinitely with increasing initial drop diameter.

The critical initial drop diameter, above which the exit velocity is constant, is only 0.020 in. even for a 250-in. nozzle. A practical injector with a pressure drop of only 5–10 psi such as that allowed in an MHD conversion system provides few drops this small, and the operating regime of interest is, therefore, on the constant-velocity portion of the curves. To be sure of being in this region, an initial drop diameter of 0.05 in. is used in the subsequent computations.

Conformity with the exposure-time requirement of the Weber number = 6 criterion is checked at this point. Figure 9 presents the variation of drop diameter with distance in the 50-in. nozzle. The 0.05-in. drop starts to

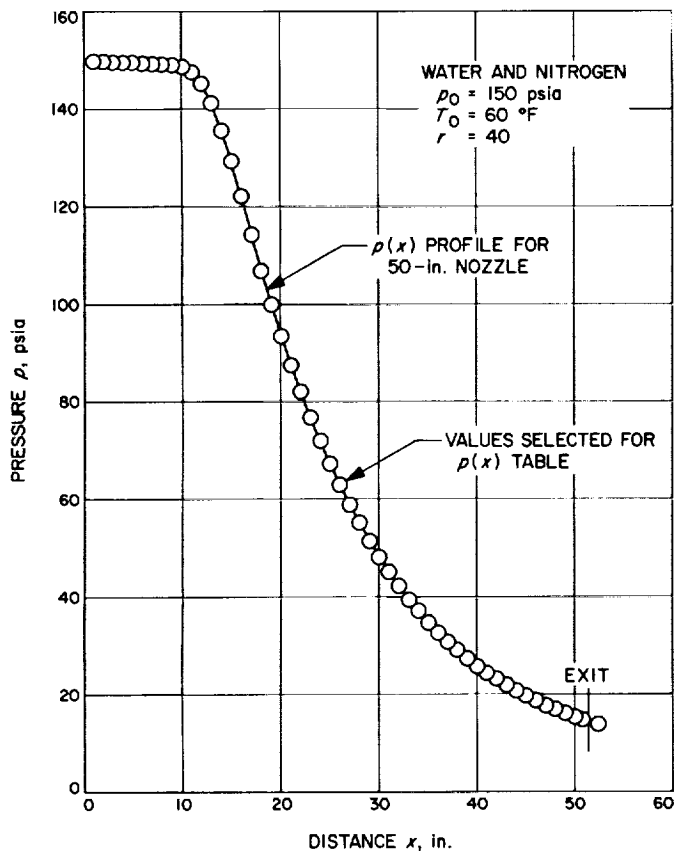


Fig. 7. Theoretical pressure profile for experimental nozzle and tabulated values employed in real-flow analysis

break up 10 in. from the inlet and completes its breakup to 0.011-in. diam at 18 in. from the inlet, 4 in. upstream of the throat. The elapsed time from injection can be obtained by integrating  $dx/V_i$  using the computer output values of  $x$  and  $V_i$ . The drop diameter as a function of time from injection is shown in Fig. 10. The drop diameter is reduced from 0.05 to 0.025 in. in 5 ms, and to 0.011 in. in 15 ms. The natural oscillation period of the 0.05-in. drop is 4 ms, and of the 0.011-in. drop 0.4 ms. Thus, the exposure time is adequate for the Weber number = 6 criterion to be valid in the 50-in. nozzle, but probably inadequate in a 10-in. nozzle.

Finally, the optimum nozzle length can be determined. Figure 11 presents the exit velocity with friction included,  $\bar{V}_\delta$ , as a function of nozzle length. For a flow rate of 160 lbm/s, the exit velocity increases rapidly with increasing length (because of decreasing slip) until a length of about 25 in. is reached. The velocity attains its maximum at a length of about 50 in. and then slowly decreases because of increasing friction. For 10 lbm/s, the optimum length is 12 in. and for 1000 lbm/s, it is about 80 in.,

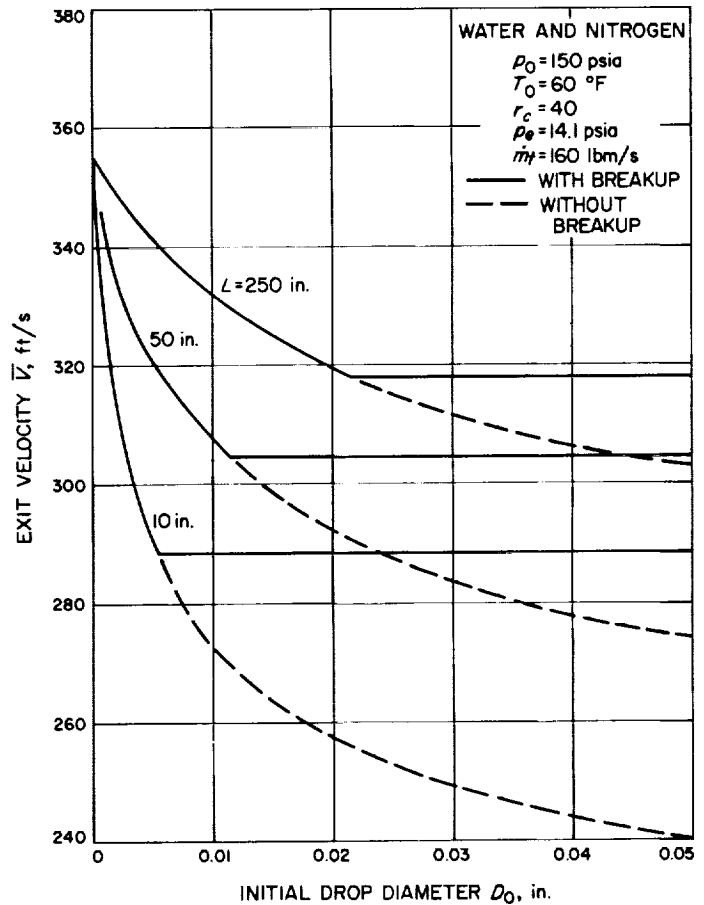


Fig. 8. Effect of length and initial drop diameter on exit velocity, with and without breakup

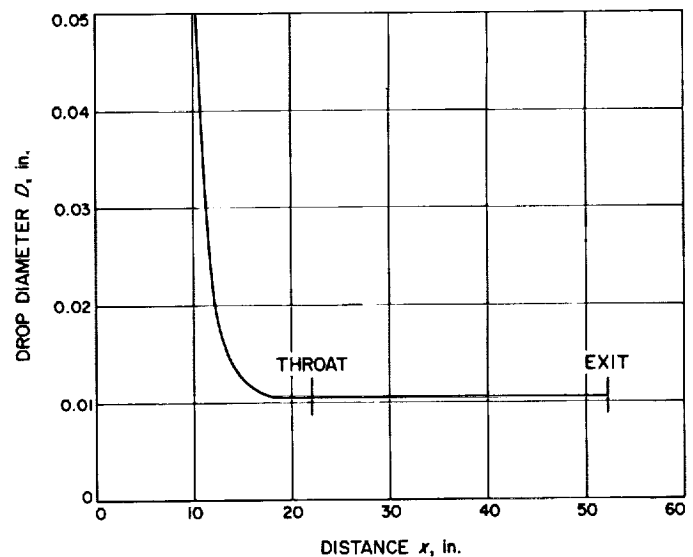


Fig. 9. Variation of drop diameter with distance from inlet

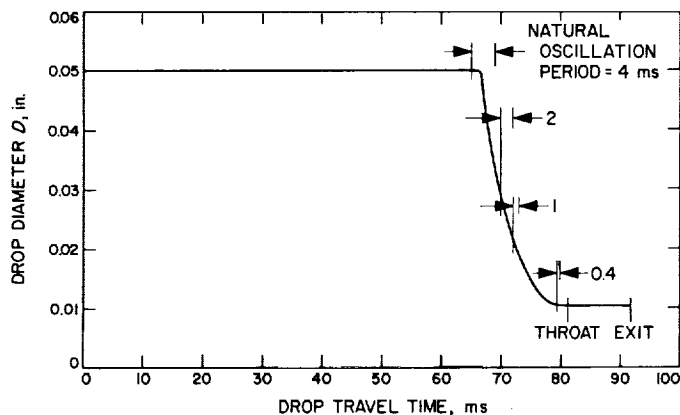


Fig. 10. Variation of drop diameter with travel time

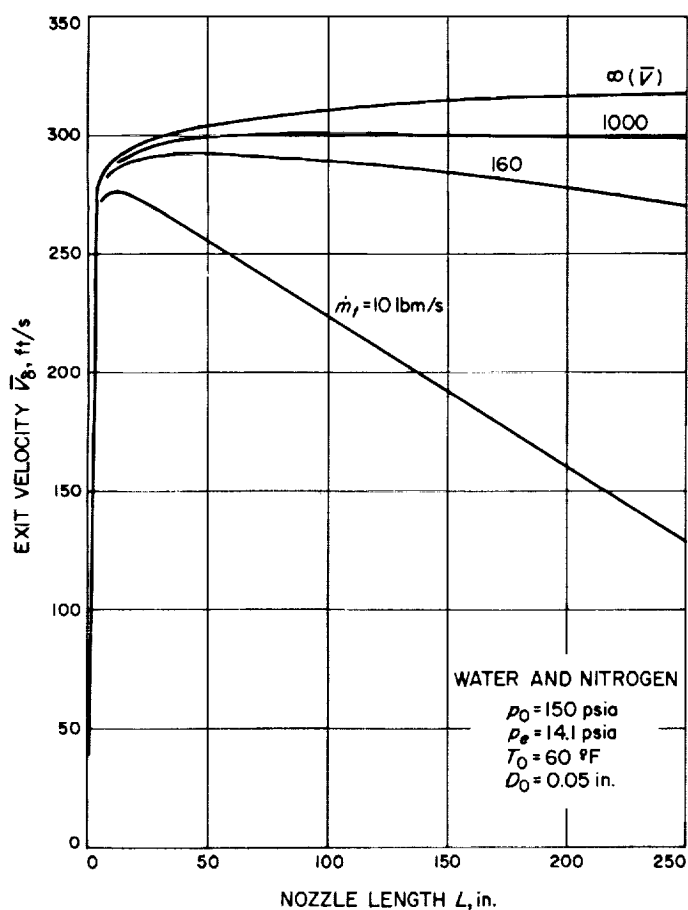


Fig. 11. Effect of nozzle length and flow rate on exit velocity with friction

although the cone angles would be excessive in the latter case, requiring lengthening the nozzle to perhaps 120 in. For infinite flow rate, the friction loss vanishes and the velocity increases indefinitely with length; the curve for this case is the free-stream velocity  $\bar{V}$ .

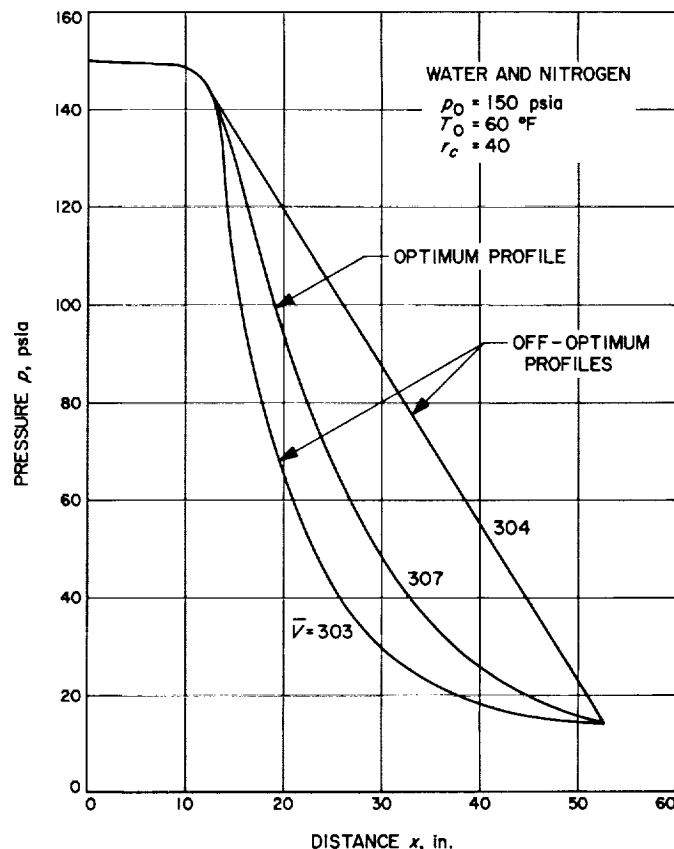


Fig. 12. Optimum and off-optimum pressure profiles and corresponding exit velocities

To illustrate the sensitivity of nozzle performance to departure from the optimum contour, Fig. 12 shows two pressure profiles which are markedly different from the optimum one. The exit velocity  $\bar{V}$  for each profile is indicated. The effect is small: the exit velocity is reduced only 1% with the off-optimum profiles. Because of this insensitivity to the  $p(x)$  profile, any reasonable approximation to  $p(x)$  can be employed in the computer programs. A convenient source of a  $p(x)$  profile for a given nozzle is the isentropic  $A(p)$  curve substituted into the  $A(x)$  profile for the nozzle.

Figures 13, 14, and 15 illustrate some of the details of the flow in the 50-in. nozzle. The variation of gas and liquid velocity with distance is shown in Fig. 13. The initial velocities are 7.3 ft/s, but a slip velocity of 12 ft/s is established within the first inch of travel. The velocities then increase slowly to about 35 ft/s for the gas and 20 ft/s for the liquid at a distance of 10 in. from the entrance. Rapid acceleration begins at this point, and the gas and liquid reach velocities of 235 and 165 ft/s,

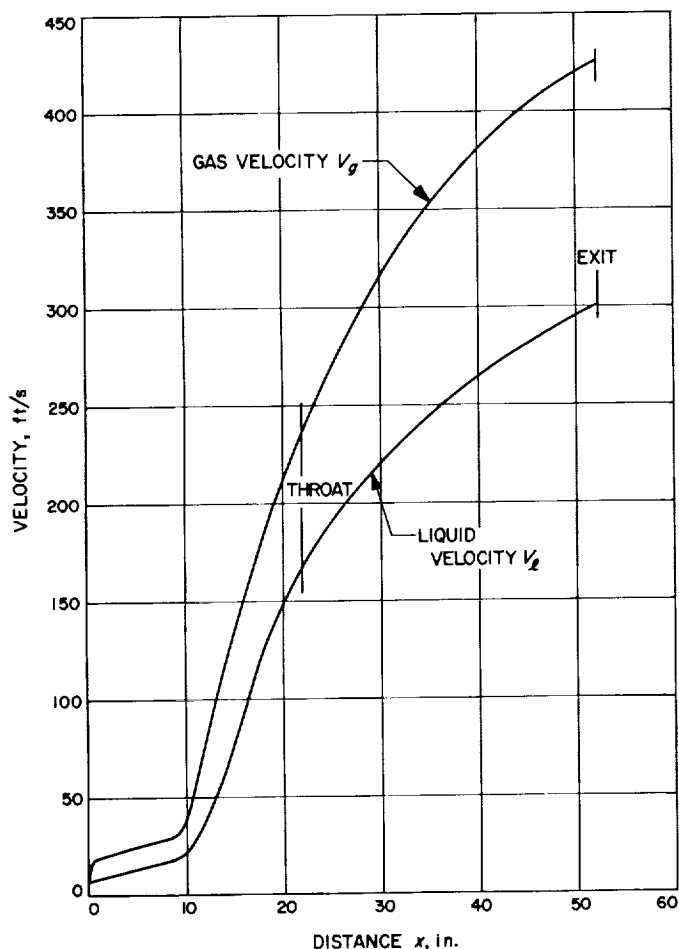


Fig. 13. Variation of liquid and gas velocities with distance

respectively, at the throat and 425 and 300 ft/s, respectively, at the exit.

Figure 14 presents the temperature variation through the nozzle. Beginning with equal temperatures, the gas and liquid leave the nozzle with a 10°F temperature difference.

The void fraction  $r_a/(1 + r_a)$  is shown in Fig. 15. The void fraction begins at 0.5, varies between 0.48 and 0.56 during the initial stages of acceleration and drop breakup, and rises to 0.94 at the exit.

## V. Comparison With Experiment

### A. Nitrogen–Water Tests in the 50-in. Nozzle

1. *Construction and test procedure.* An experimental nozzle was built whose contour was derived in Section IV

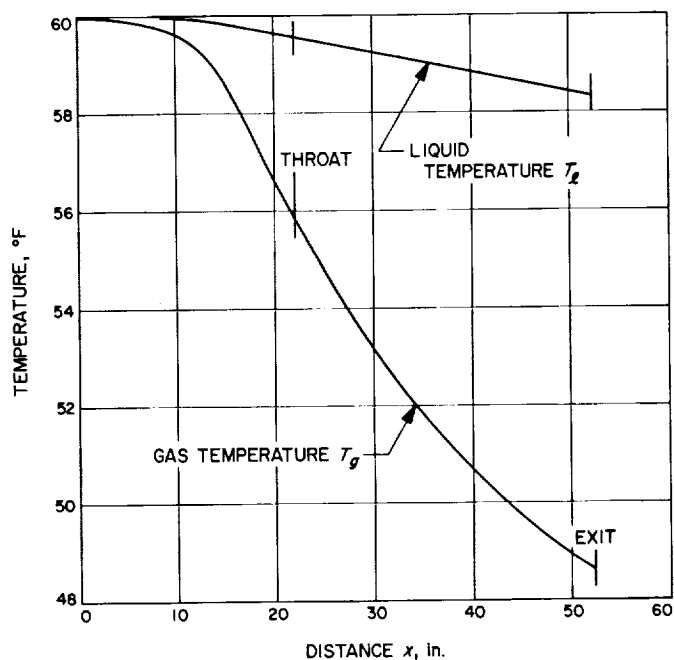


Fig. 14. Variation of liquid and gas temperatures with distance

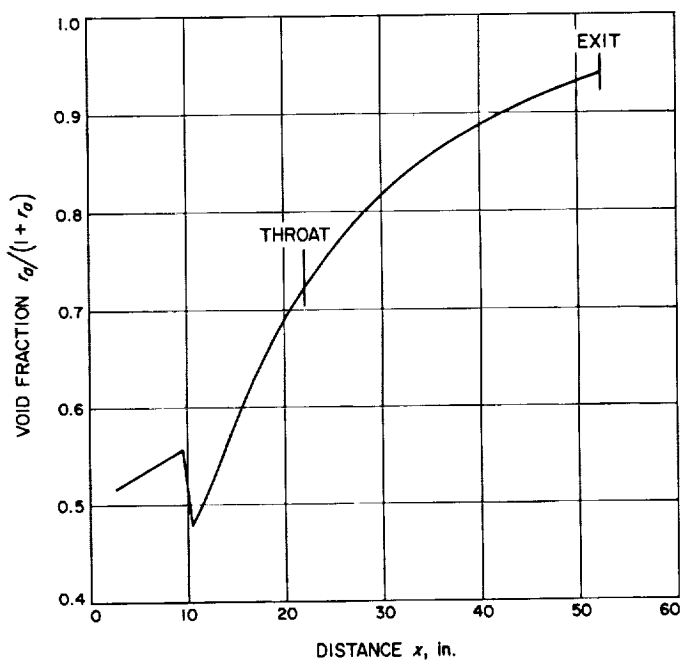


Fig. 15. Variation of void fraction with distance

(Fig. 6). Figure 16 is a drawing of the nozzle and injector, which were made of 6061 aluminum alloy, and Fig. 17 shows the details of the injection tubes. The nozzle had an entrance diameter of 14.5 in. and converged at a 20-deg half-angle to a diameter of 4.2 in. at a distance of

x	y	x	y	x	y	x	y	x	y	x	y
0	2.100	5.000	1.624	10.000	1.604	15.000	1.693	20.000	1.842		
0.500	1.961	5.500	1.613	10.500	1.610	15.500	1.705	20.500	1.859		
1.000	1.881	6.000	1.604	11.000	1.617	16.000	1.717	21.000	1.876		
1.500	1.821	6.500	1.598	11.500	1.625	16.500	1.730	21.500	1.893		
2.000	1.774	7.000	1.593	12.000	1.633	17.000	1.744	22.000	1.911		
2.500	1.733	7.500	1.591	12.500	1.642	17.500	1.759	22.500	1.930		
3.000	1.701	8.000	1.590	13.000	1.651	18.000	1.775	23.000	1.950		
3.500	1.675	8.500	1.591	13.500	1.661	18.500	1.791	23.500	1.970		
4.000	1.654	9.000	1.593	14.000	1.671	19.000	1.808	24.000	1.992		
4.500	1.637	9.500	1.598	14.500	1.682	19.500	1.824				

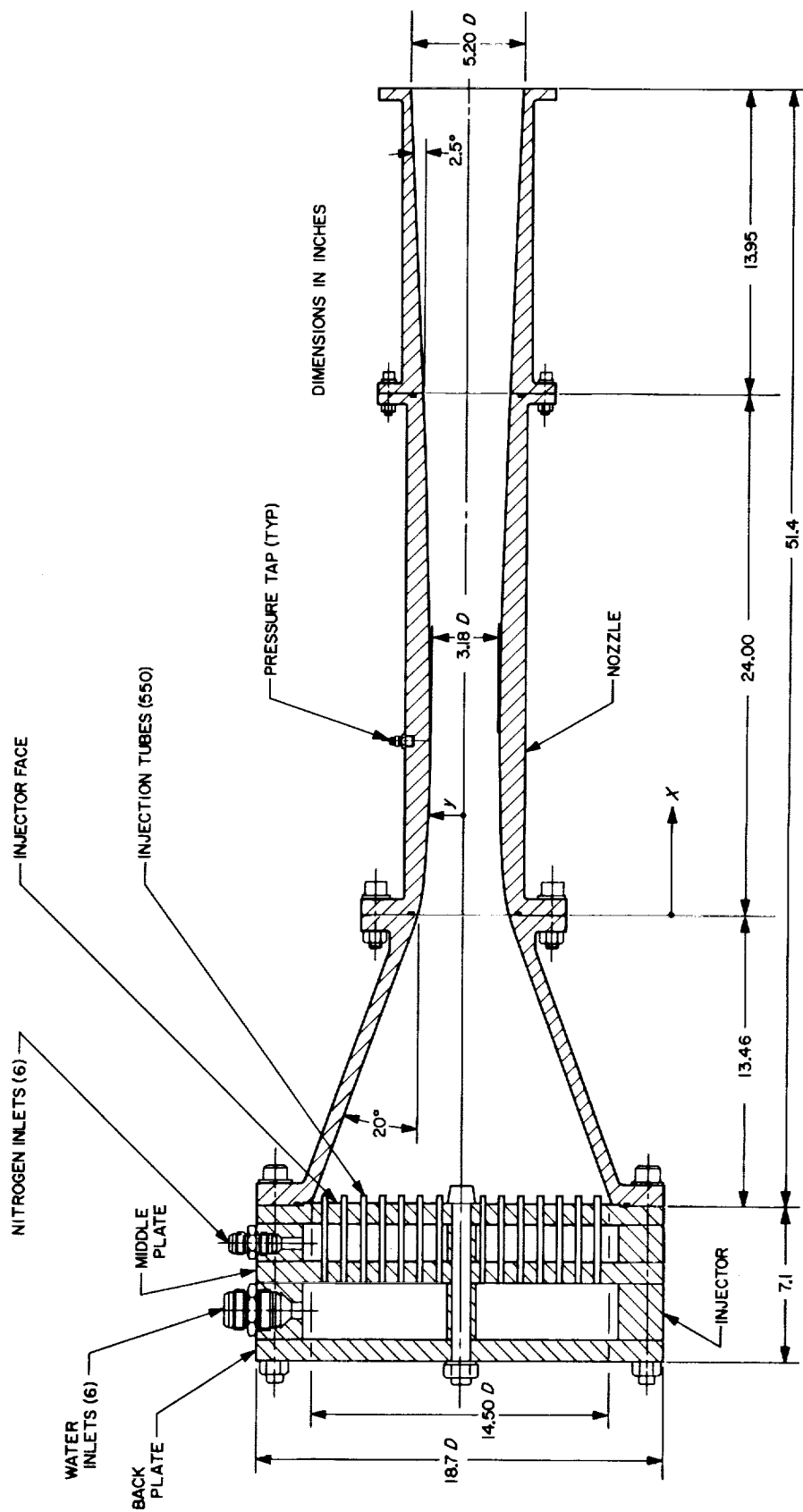


Fig. 16. 50-in. nozzle and injector

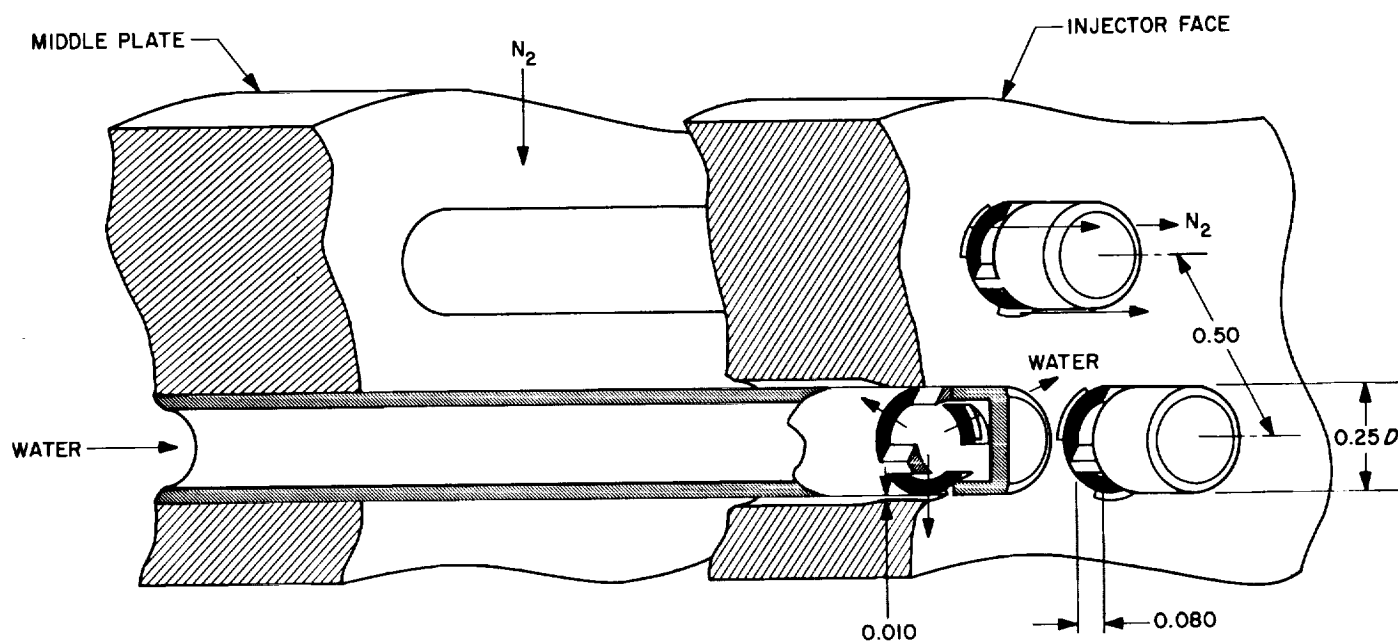


Fig. 17. Injection orifice details

13.5 in. from the inlet. The nozzle then followed the tabulated curve to a throat diameter of 3.18 in. at 21.5 in. from the inlet, continued the tabulated curve to a diameter of 3.98 in. at 37.5 in. from the inlet, and diverged at a half-angle of 2.5 deg to an exit diameter of 5.2 in. at 51.4 in. from the inlet. The nozzle was fabricated in three sections, which were bolted together and sealed with O-rings. A row of pressure taps was provided for measurement of the pressure profile.

The injector consisted of 550 0.25-in.-diam tubes projecting through slotted holes in the injector face. Water entered the injector through six 1.5-in.-diam inlets, flowed into the space between the middle and back plates, entered the injection tubes (Fig. 17), and left parallel to the injector face through three orifices at the tip of each tube. Nitrogen entered the injector through six 0.75-in.-diam inlets, flowed into the space surrounding the tubes between the middle plate and injector face, entered slots in the injector face, and flowed axially into the nozzle at three points around each tube in line with the water jets. The water orifices at the end of each tube consisted of slots 0.08 in. wide at three places around the circumference of each tube, with the upstream edge flush with the injector face; the slots in the initial test series were 0.040 in. wide, with the upstream edge 0.040 in. from the injector face. The nitrogen orifices were three slots in the tube support holes, each 0.010 in. wide radially,

occupying 60 deg of the circumference and extending 1.0 in. axially to join with a 0.28-in.-diam entrance annulus. The slots in the initial test series were 0.005 in. wide. A 1.0-in.-diam bolt in the center extended through the three plates to reduce deflection. Pressure taps were provided in the water and nitrogen manifolds for determining injection pressure.

The nozzle was mounted on a parallelogram thrust stand, and the thrust was measured by a strain-gage force transducer mounted between the nozzle and a rigid support. Water and nitrogen flowed through tubes connected to overhead supply pipes through flexible hoses. Water was supplied from a pump capable of delivering 180 lb/s of water at 500 psi. Nitrogen was supplied from twelve 25-ft<sup>3</sup>, 2200-psi cylinders at flow rates up to 10 lb/s. The flow leaving the nozzle was deflected downward into a sump from which the water returned to the pump while the nitrogen exhausted to the atmosphere. Figure 18 shows the nozzle in operation during a test.

The nozzle was operated at inlet pressures from 110 to 230 psia, water flow rates from 90 to 180 lb/s, and nitrogen flow rates from 2.5 to 9.5 lb/s. The mean exit velocity  $\bar{V}$  ranged from 250 to 540 ft/s, and the exit Mach number  $\bar{V}(\rho_1 r_a/p)^{1/2}/(1+r_a)$  (Ref. 25, p. 7) ranged from 2.2 to 2.5. The nozzle sounded like an ordinary gas nozzle and had a 90-dB sound level. The pressure at the nozzle inlet

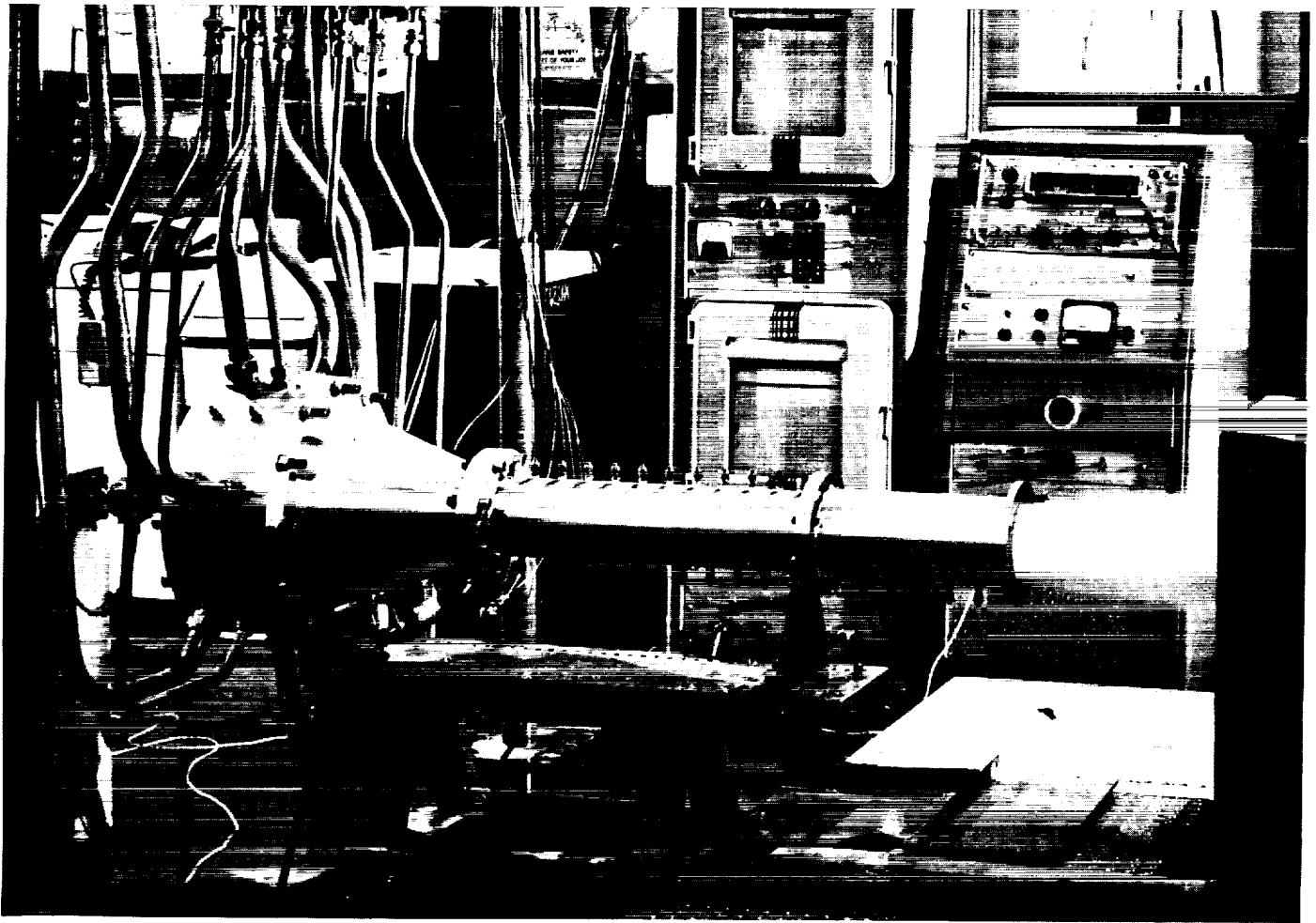


Fig. 18. Experimental nozzle in operation

fluctuated by no more than 1 psi according to measurements made with a transducer having a frequency response to 1000 Hz. The exhaust jet was white and opaque, with some axial striations visible around the circumference. The jet had a sharp boundary as it left the nozzle, but the boundary became diffuse a few inches downstream as a result of entrainment of atmospheric air.

Figure 19 is a 1- $\mu$ s flash photograph of the jet. The motion is stopped (0.003-in. travel at 300 ft/s), but the appearance differs little from that seen by the eye. The striations in the jet show more clearly; they are probably remnants of the injector pattern.

The difference between the water injection pressure and the nozzle inlet pressure, the latter measured at a tap 3 in. downstream from the injector face, is plotted as a function of water flow rate in Fig. 20. The pressure drop was 14 psi at the maximum flow rate of 180 lb/s with the

0.08-in. orifice width and 36 psi with the 0.04-in. orifice width, and the pressure drop was proportional to the 1.5 power of the flow rate. The nitrogen injection pressure drop is shown in Fig. 21. The range of pressure drops for the tests was 10 to 60 psi for the 0.010-in. slots and 40 to 170 psi for the 0.005-in. slots. Liquid Freon 1301 ( $\text{CBrF}_3$ ) was used in place of nitrogen in one test, and Fig. 22 shows the measured Freon injection pressure drops, which ranged from 7 to 25 psi.

The flow rates given as  $\dot{m}_i$  and  $\dot{m}_g$  in Figs. 20-22 should more strictly be labeled the component flow rates  $\dot{m}_b$  and  $\dot{m}_a$ , respectively. The solubility of nitrogen in water, however, is low enough that the differences are negligible, and it has been customary to employ  $\dot{m}_i$  for  $\dot{m}_b$  and  $\dot{m}_g$  for  $\dot{m}_a$ . Similarly, the mixture ratio  $r = \dot{m}_i/\dot{m}_g$  has customarily been employed where the component ratio  $r_c = \dot{m}_b/\dot{m}_a$  is really meant, and this practice will be followed in the remainder of the report.



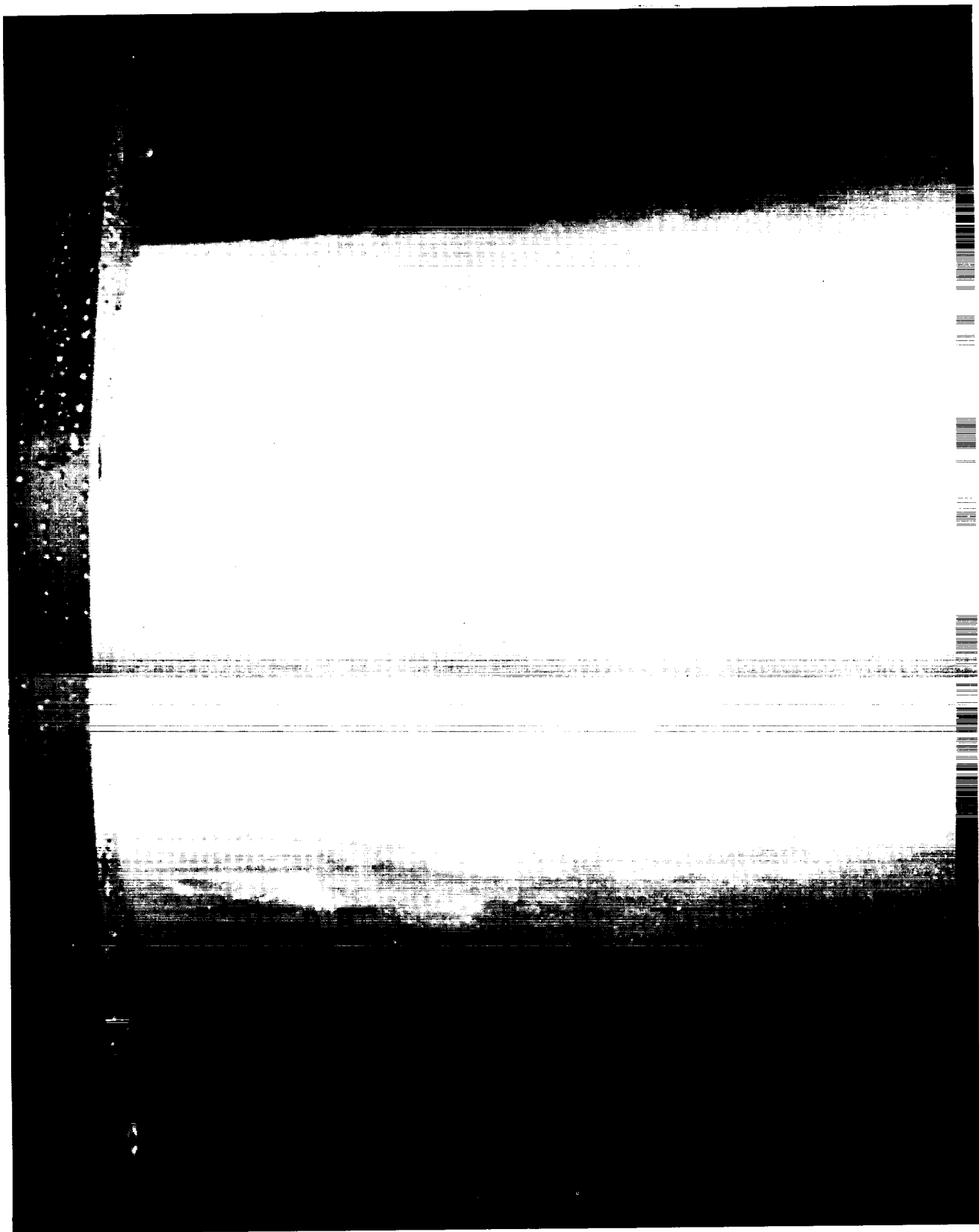


Fig. 19. Exit jet at 1.0- $\mu$ s exposure

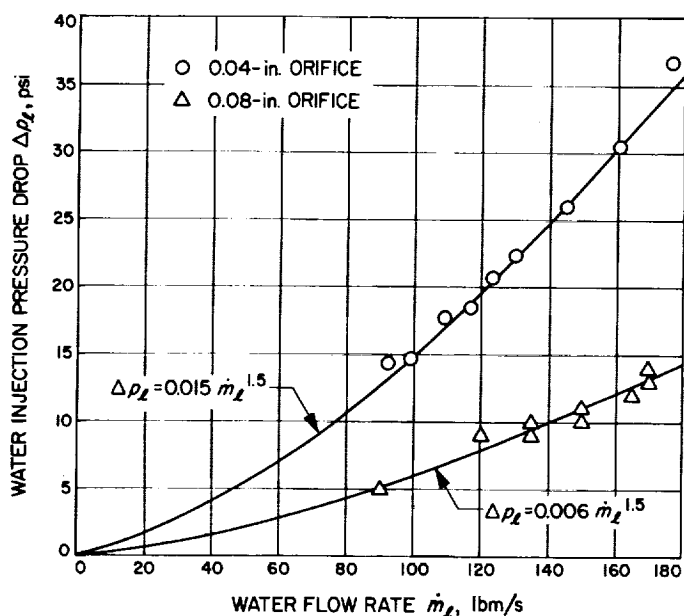


Fig. 20. Water injection pressure drop

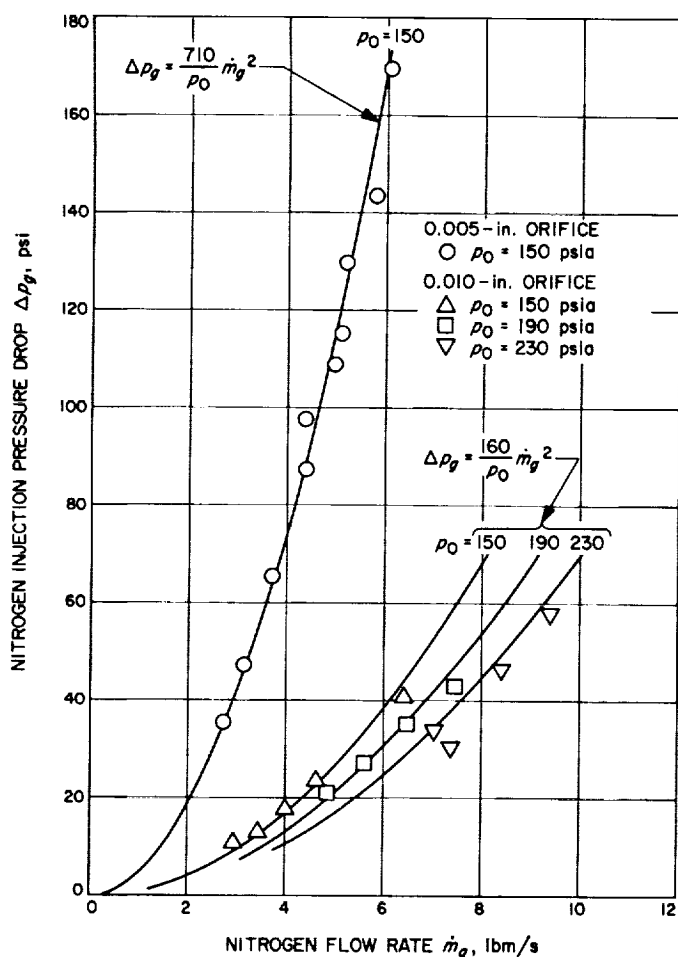


Fig. 21. Nitrogen injection pressure drop

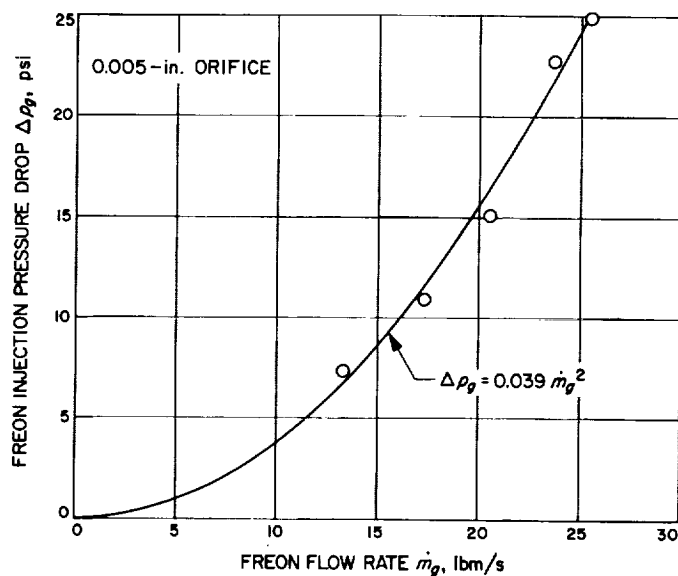


Fig. 22. Freon injection pressure drop

The gas injection pressure drops and gas flow rates in the 50-in. nozzle were too low to provide atomization of a significant fraction of the water to drops of 0.02-in. diameter or less, thus making the nozzle dependent on drop breakup during expansion. Lack of atomization on injection was verified in an experiment in which a single injector element with 0.04-in. water orifices and 0.005-in. nitrogen slots was operated over the range of nozzle mixture ratios inside a 3-in.-diam transparent tube maintained at 150-psi nitrogen pressure. The water jets were observed to be unaffected by the impinging nitrogen jets except for being deflected 5 to 10 deg away from the injector face. The flow from the injector of the 50-in. nozzle consisted, therefore, of a uniformly distributed, but only coarsely atomized, dispersion of water drops in nitrogen. A drop-flow, rather than bubble-flow, regime existed because the volume ratio of gas to liquid at the nozzle entrance ranged from 1 to 4.

Based on the apparent lack of atomization at the inlet of this nozzle, the initial drop diameter appropriate for analyzing the nozzle with the real-flow program would be any value large enough to exceed  $We = 6$  early in the nozzle and require drop breakup. Computer runs were made with various initial drop diameters, and a diameter of 0.05 in. was found sufficient for breakup in all cases, and for exit velocities that were independent of further increases in initial drop diameter, as illustrated in Fig. 8. The same approach was employed in selecting initial drop diameters for analyzing the other experimental nozzles to be discussed; a diameter was selected in each

case which gave results on the flat portion of the velocity-versus-diameter curve.

**2. Pressure profile.** Pressures were measured at seven stations along the nozzle during runs made at 150-psia inlet pressure. The measurements made at a mixture ratio of 39.1 are compared with theory for  $r = 40$  in Fig. 23, and show close agreement. The theoretical curve requires some additional explanation. The program does not give  $p(x)$  for a prescribed nozzle contour, but it does give area as a function of pressure,  $A(p)$ , and the area, like the velocity, is insensitive to the  $p(x)$  profile supplied (see Fig. 12). Thus, the  $A(p)$  values printed are accurate for the actual nozzle, which has a  $p(x)$  profile differing little from the one prescribed in the program. A valid theoretical  $p(x)$  curve for the experimental nozzle can, therefore, be obtained by converting the printed  $A(p)$  to  $x(p)$  values, using the  $A(x)$  values for the experimental nozzle, and this procedure was the origin of the theoretical curve in Fig. 23. The measured pressures are within 1 psi of the theoretical curve.

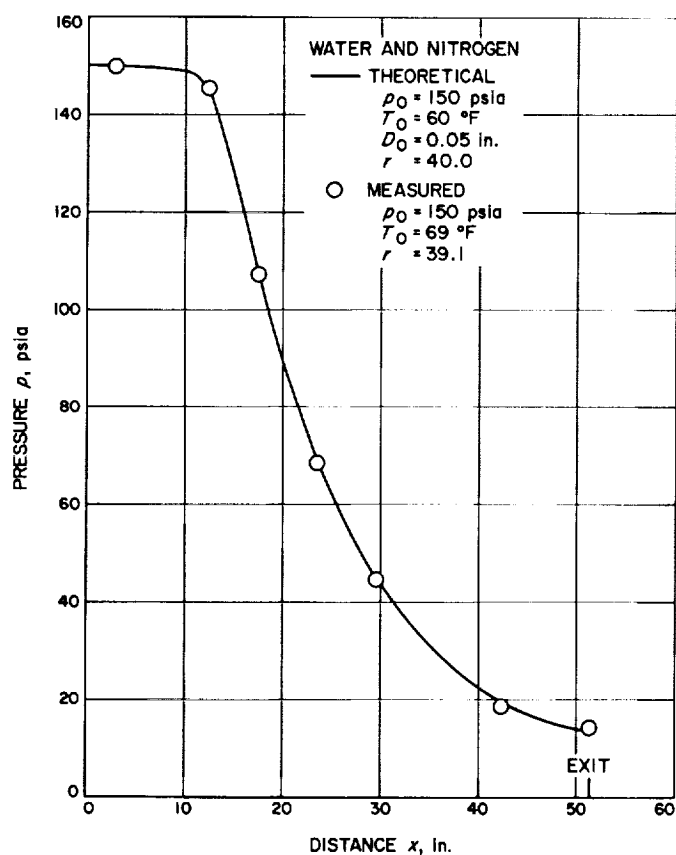


Fig. 23. Comparison of theoretical and experimental pressure profiles

The theoretical and experimental variations of pressure with mixture ratio at a fixed station  $x = 29.46$  in. are compared in Fig. 24. The measured values are within 1 psi of theoretical from  $r = 15$  to  $r = 70$ , falling below at low mixture ratios and above at high mixture ratios, probably in response to the nozzle exit behavior discussed next.

Figure 25 shows the theoretical and experimental variation of nozzle exit pressure with mixture ratio for inlet pressures of 150 and 230 psia. The experimental pressure was measured with a 0.04-in.-diam tap located 0.2 in. upstream of the nozzle exit. The theoretical exit pressure

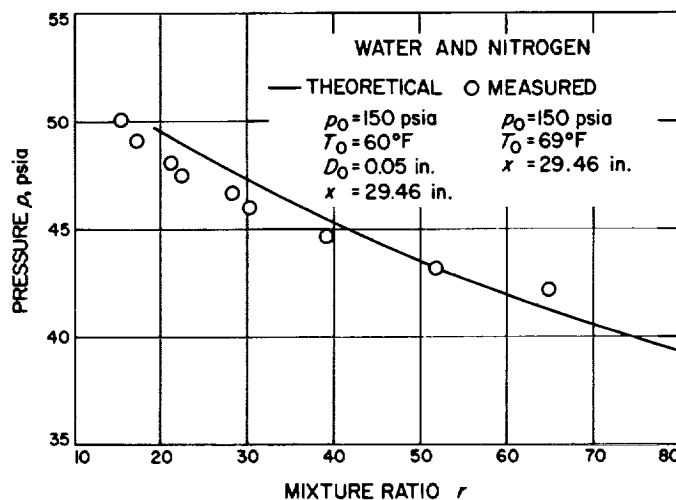


Fig. 24. Comparison of theoretical and experimental variation of pressure with mixture ratio 21 in. upstream of exit

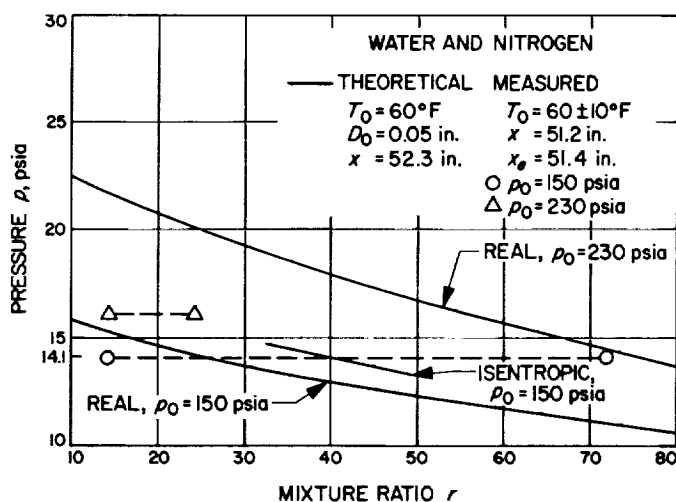


Fig. 25. Comparison of theoretical and experimental variation of pressure with mixture ratio at exit

for 150-psia inlet pressure ranges from 16 psia at  $r = 10$  to 11 psia at  $r = 80$ , but the measured pressure is constant at 14.1 psia, the laboratory atmospheric pressure. At 230-psia inlet pressure, the theoretical exit pressure ranges from 22 psia at  $r = 10$  to 14 psia at  $r = 80$ , but the measured pressure is constant at 16 psia up to the maximum mixture ratio of 25 attainable at 230 psia. Thus, in practice, the exit pressure tends to remain equal to atmospheric pressure, at least at the wall, even though the flow is nominally supersonic and independent of atmospheric pressure.

3. **Flow rate.** Table 2 presents the theoretical total flow rates for isentropic flow, real flow without friction, and real flow with friction for mixture ratios from 10 to 80 at nozzle inlet pressures of 150, 190, and 230 psia. The flow rates are plotted as a function of mixture ratio for each pressure in Figs. 26, 27, and 28.

The flow rate for real flow without friction is the highest; with friction, the flow rate is 2% lower, and for

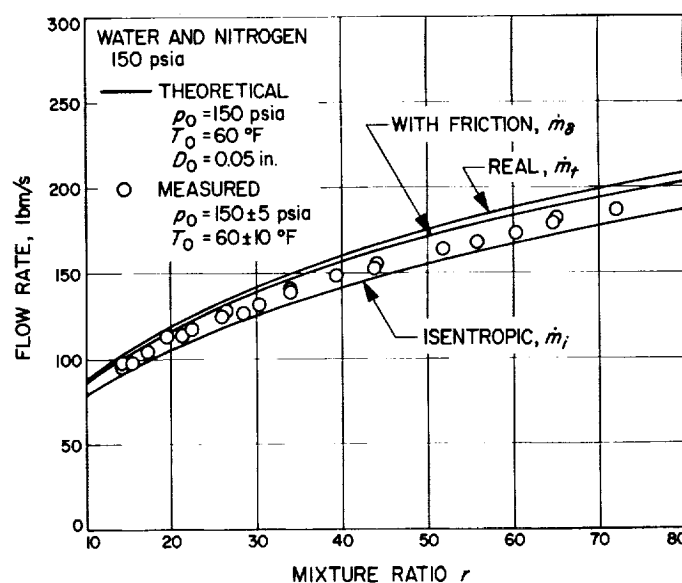


Fig. 26. Comparison of theoretical and experimental flow rates at 150-psia nozzle inlet pressure

Table 2. Theoretical performance of 50-in. nozzle with water and nitrogen<sup>a</sup>

Inlet pressure $p_0$ psia	Mixture ratio $r$	Isentropic-flow rate $\dot{m}_i$ lbm/s	Real-flow rate $\dot{m}_r$ lbm/s	Flow with friction $\dot{m}_g$ lbm/s	Isentropic velocity $V_i$ ft/s	Real velocity $\bar{V}$ ft/s	Velocity with friction $\bar{V}_g$ ft/s
150	10	78.5	87.1	85.9	642.6	556.7	539.8
	20	106.0	119.0	117.1	476.2	407.9	393.4
	30	126.0	142.3	139.7	400.3	342.6	329.5
	40	142.0	160.4	157.4	355.1	304.8	292.4
	50	155.5	175.2	171.9	324.5	279.7	267.9
	60	167.1	187.9	184.0	302.2	261.8	250.2
	70	177.2	198.8	194.6	285.1	248.2	236.9
	80	186.3	208.6	203.8	271.5	237.5	226.4
190	10	98.9	108.4	106.9	676.1	595.9	575.8
	20	132.8	146.8	144.3	502.9	439.8	422.9
	30	157.2	174.2	171.1	424.2	371.2	355.8
	40	176.5	195.3	191.7	377.4	331.4	316.8
	50	192.5	212.7	208.3	345.8	305.1	291.0
	60	206.2	227.2	222.5	322.8	286.2	272.4
	70	218.1	239.9	234.4	305.3	272.0	258.4
	80	228.7	251.0	245.2	291.3	260.8	247.4
230	10	119.1	129.4	127.5	702.7	627.3	604.8
	20	159.1	174.0	171.0	524.5	465.7	446.6
	30	187.5	205.2	201.5	443.7	394.7	377.0
	40	209.8	228.9	224.3	395.8	353.5	336.7
	50	228.1	248.3	242.8	363.6	326.3	309.9
	60	243.7	265.0	259.1	340.2	306.8	290.8
	70	257.2	278.8	272.5	322.3	292.1	276.3
	80	269.0	291.2	284.0	308.2	280.5	264.9

<sup>a</sup> $T_0 = 60^\circ\text{F}$ ,  $p_e = 14.1$  psia,  $A_t = 7.942$  in.<sup>2</sup>,  $D_0 = 0.05$  in.

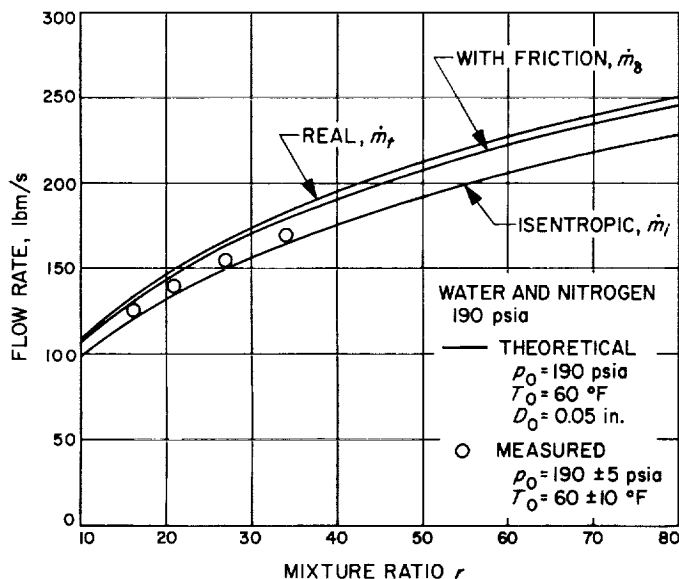


Fig. 27. Comparison of theoretical and experimental flow rates at 190-psia nozzle inlet pressure

isentropic flow it is about 10% lower than for frictionless real flow. The isentropic flow rate is lowest because, with no slip, the gas velocity is lowest and, with fixed throat area, the gas flow rate is lowest. At fixed mixture ratio, this results in the lowest total flow rate.

Table 3 presents the experimental flow rates, and they are plotted with the theoretical curves in Figs. 26, 27, and 28. The experimental flow rates are about 3% lower than the theoretical values (real flow with friction) at the lowest mixture ratios tested and about 5% lower than theoretical at the highest ratios tested. The fact that the experimental flow rates are between the isentropic and real-flow values probably reflects the underestimation of liquid drag, discussed in Section II, because of the assumption of  $We = 6$  diameter for all the drops and the use of the solid sphere drag coefficient.

**4. Exit velocity.** Table 2 also presents the theoretical exit velocities for isentropic flow, real flow without friction, and real flow with friction. The velocities are plotted in Figs. 29, 30, and 31. The isentropic velocity is highest; the real velocity without friction is 10 to 15% lower, and friction reduces the velocity another 3%.

The experimental exit velocities are given in Table 3 and plotted with the theoretical curves in Figs. 29, 30, and 31. The experimental exit velocities are 3 to 5% higher than theoretical (real flow with friction), the difference being attributed to the underestimation of drop drag.

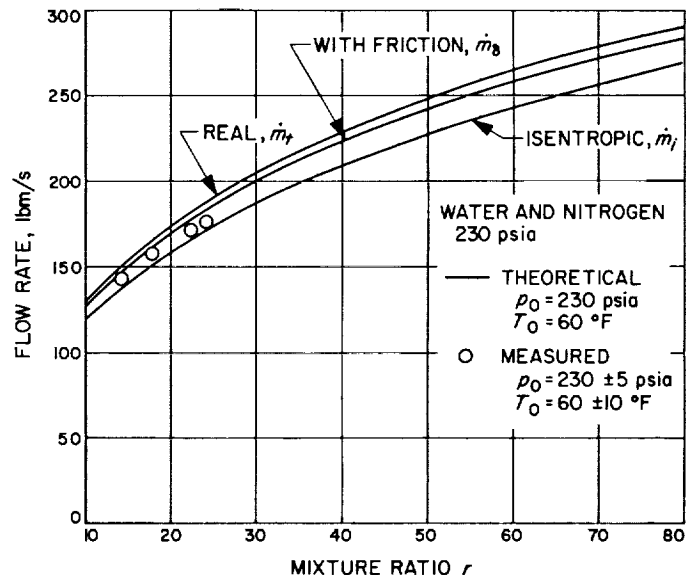


Fig. 28. Comparison of theoretical and experimental flow rates at 230-psia nozzle inlet pressure

The experimental exit velocity is greater than theoretical in this nozzle by an amount about equal to the velocity loss from friction. Thus, the real velocity without friction gives, fortuitously, the best agreement with experiment, predicting the measured values within 2%. Advantage was taken of this fact in the cycle studies presented in Ref. 27, where the nozzle exit velocities employed were the real-flow frictionless values.

## B. Freon–Water Experiment

Six runs were made with liquid Freon 1301 ( $CBrF_3$ ) in place of nitrogen to verify that the gas phase could be produced by contact vaporization at the inlet of a two-phase nozzle, an important requirement in MHD power systems. The results showed that complete vaporization occurred, in that the data agreed as well with the theory as in the nitrogen–water tests.

**1. Flow rate.** Table 4 presents the theoretical and measured flow rates at the six mixture ratios and inlet temperatures obtained. The flow rates are plotted as a function of mixture ratio in Fig. 32. Real flow without friction is the highest, real flow with friction 2% lower, and isentropic flow another 4% lower. The experimental flow rates are about 2% lower than theoretical (real flow with friction).

**2. Exit velocity.** Table 4 also presents the theoretical and measured exit velocities, which are plotted as a

Table 3. Measured performance of 50-in. nozzle with water and nitrogen<sup>a</sup>

Test series	Inlet pressure $p_0$ psia	Nitrogen flow rate $\dot{m}_N$ lbm/s	Water flow rate $\dot{m}_W$ lbm/s	Total flow rate $\dot{m}_t$	Mixture ratio $r$	Thrust $F$ lbf	Exit velocity $\bar{V}$ ft/s
1	$150 \pm 5$	6.46	92	98	14.2	1426	468
		5.52	107	113	19.4	1424	405
		4.68	123	128	26.3	1432	360
		4.04	137	141	33.9	1430	326
		3.49	153	156	43.8	1441	297
		2.73	176	179	64.5	1441	259
		2.56	184	187	71.9	1464	252
2	$150 \pm 2$	6.03	92	98	15.3	1424	468
		5.75	99	105	17.2	1402	430
		5.16	109	114	21.1	1448	409
		5.07	113	118	22.3	1418	387
		4.35	123	127	28.3	1418	359
		4.32	130	134	30.1	1424	342
		3.70	145	149	39.2	1424	307
		3.12	161	164	51.6	1424	279
3	$150 \pm 5$	2.71	176	179	64.9	1424	256
		6.40	90	96	14.1	1450	486
		4.65	120	125	25.8	1440	371
		4.00	135	139	33.8	1450	336
		3.44	150	153	43.6	1450	305
		2.97	165	168	55.6	1456	279
		2.83	170	173	60.1	1457	271
3	$190 \pm 5$	7.45	120	127	16.1	1940	491
		6.45	135	141	20.9	1916	437
		5.60	150	156	26.8	1914	395
		4.88	165	170	33.8	1915	362
3	$230 \pm 5$	9.40	135	144	14.4	2425	542
		8.40	150	158	17.9	2425	494
		7.39	165	172	22.3	2420	453
		7.05	170	177	24.1	2440	444

<sup>a</sup>  $T_0 = 60 \pm 10^\circ\text{F}$ ,  $p_0 = 14.1$  psia,  $A_t = 7.942$  in.<sup>2</sup>

Table 4. Theoretical and measured performance of 50-in. nozzle with water and Freon 1301 at 150 psia<sup>a</sup>

Inlet temperature $T_0$ $^\circ\text{F}$	Mixture ratio $r$	Isentropic flow rate $\dot{m}_i$ lbm/s	Real flow rate $\dot{m}_r$ lbm/s	Flow rate with friction $\dot{m}_f$ lbm/s	Isentropic velocity $V_i$ ft/s	Real velocity $\bar{V}$ ft/s	Velocity with friction $\bar{V}_f$ ft/s	Measured flow rate $\dot{m}_t$ lbm/s	Measured velocity $\bar{V}$ ft/s
46	3.97	124.8	131.5	129.6	406.4	378.1	366.3	127	372
48	4.66	131.7	138.7	136.6	384.9	357.9	346.3	134	355
51	6.38	146.2	154.7	152.2	344.8	320.7	309.5	152	315
52	7.11	151.9	160.7	158.0	332.0	308.9	297.8	155	314
53	8.79	163.6	173.1	170.0	308.0	286.9	276.0	169	284
54	11.00	177.0	187.0	183.5	284.9	266.0	255.3	—	—
55	13.66	190.6	201.1	196.9	264.6	247.9	237.4	193	247

<sup>a</sup>  $p_0 = 150.0$  psia,  $p_e = 14.1$  psia,  $A_t = 7.942$  in.<sup>2</sup>,  $D_0 = 0.05$  in.

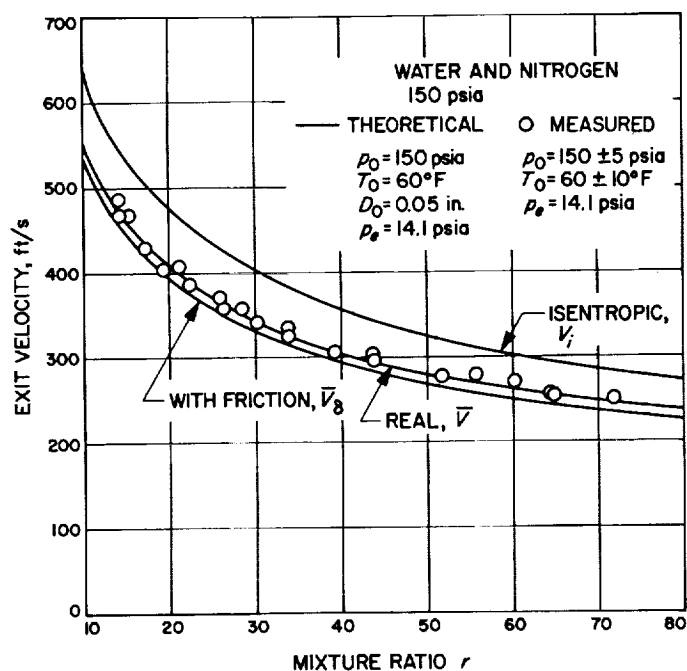


Fig. 29. Comparison of theoretical and experimental exit velocities at 150-psia nozzle inlet pressure

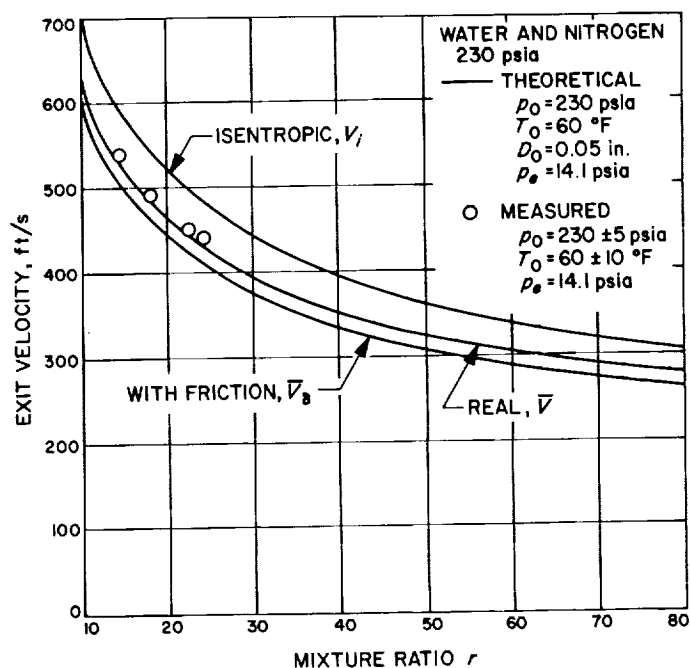


Fig. 31. Comparison of theoretical and experimental exit velocities at 230-psia nozzle inlet pressure

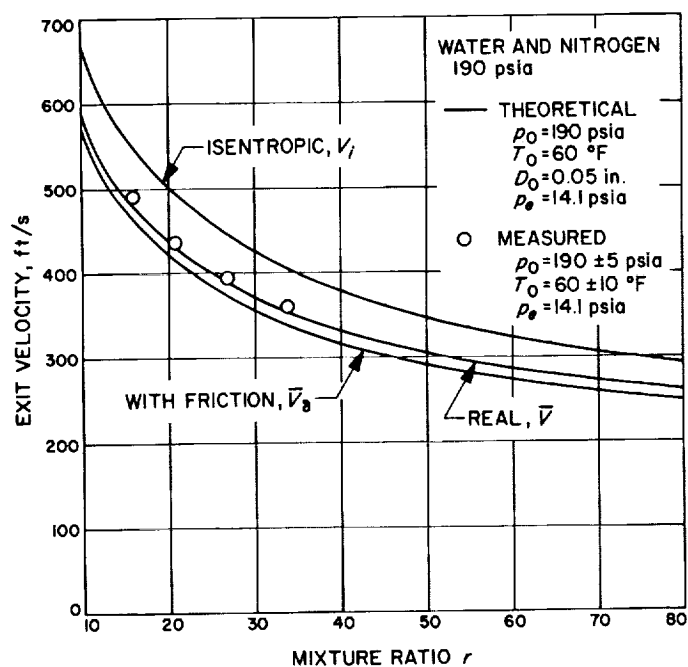


Fig. 30. Comparison of theoretical and experimental exit velocities at 190-psia nozzle inlet pressure

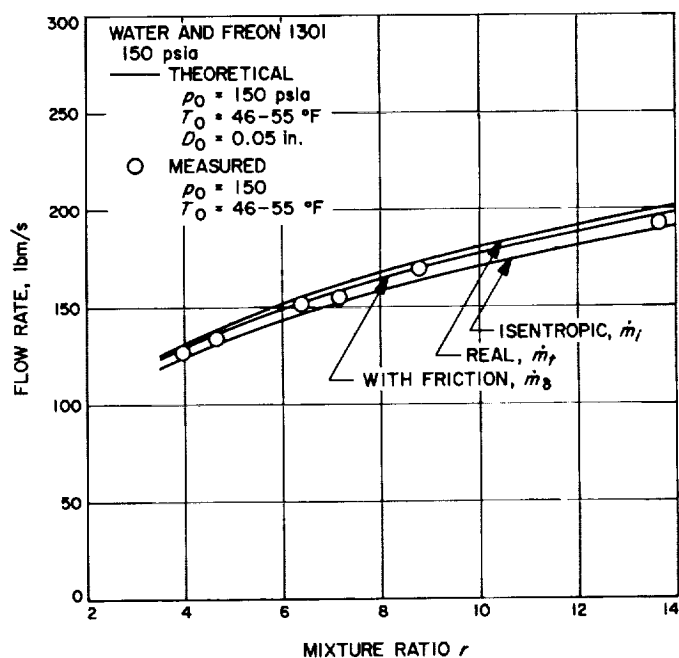


Fig. 32. Comparison of theoretical and experimental flow rates using Freon

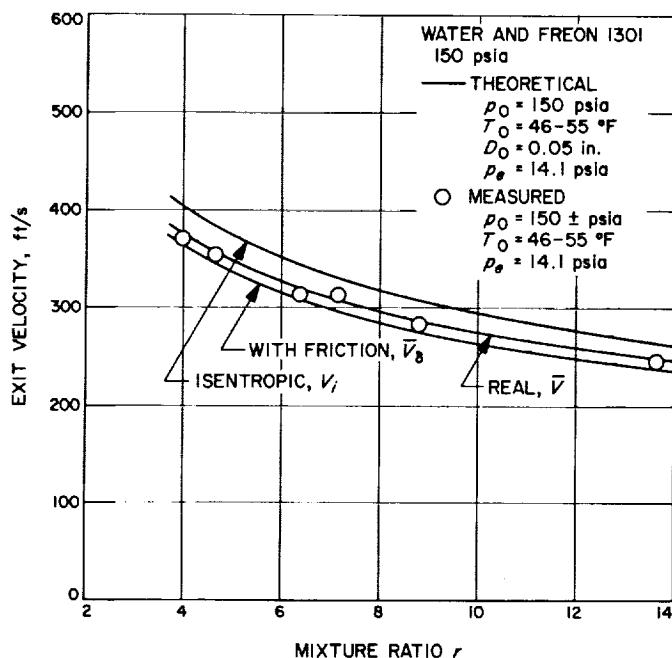


Fig. 33. Comparison of theoretical and experimental exit velocities using Freon

function of mixture ratio in Fig. 33. The exit velocity for real flow without friction is 7% below isentropic, and the velocity is reduced another 3% with friction. The measured values are 3% above theoretical (real flow with friction) and again agree best with the real frictionless

values, showing that the loss due to friction is fortuitously counterbalanced by the drop drag underestimation.

### C. Six-Inch Nozzle

Water-air experiments with a 6-in.-long two-phase nozzle at 514 psia inlet pressure and mixture ratios from 4 to 33 were reported in Ref. 1. Figure 34 is a drawing of the nozzle, which had an inlet diameter of 1.62 in., throat diameter of 0.20 in., and exit diameter of 0.53 in. The two-phase, two-component program was employed to calculate the theoretical flow rate and exit velocity of this nozzle, using the isentropic pressure profile and 0.01-in. initial drop diameter, a diameter which caused breakup in the nozzle.

1. *Flow rate.* Figure 35 compares the theoretical and experimental flow rates. The experimental flow rates are 1 to 2% lower than with the theoretical values (real flow with friction). The fact that the flow rate is closer to theoretical than in the larger nozzle is attributed to the shorter time available for drop breakup, which was only a fraction of the drop natural period. The shorter exposure time would give a drop diameter distribution with a higher mean value, more closely approaching the Weber number = 6 value.

2. *Exit velocity.* The theoretical and experimental exit velocities for the 6-in. nozzle are compared in Fig. 36 with the mean of the data represented by the dashed curve.

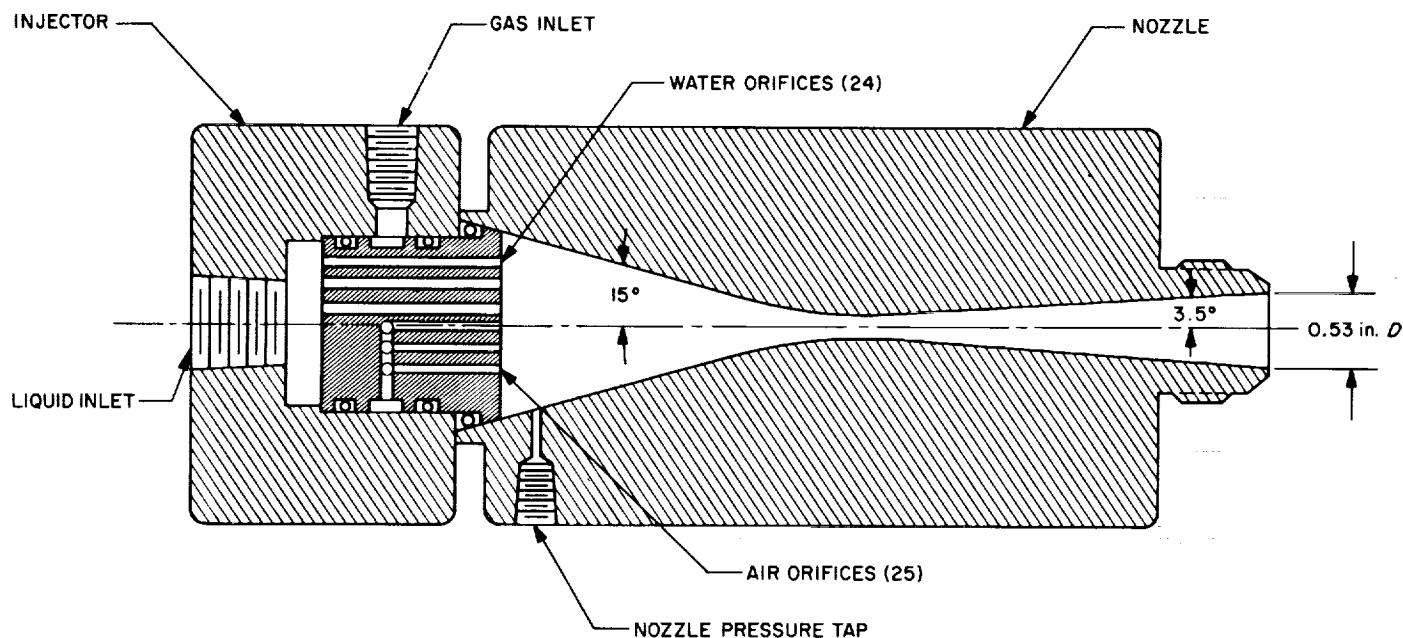


Fig. 34. 6-in. nozzle and injector



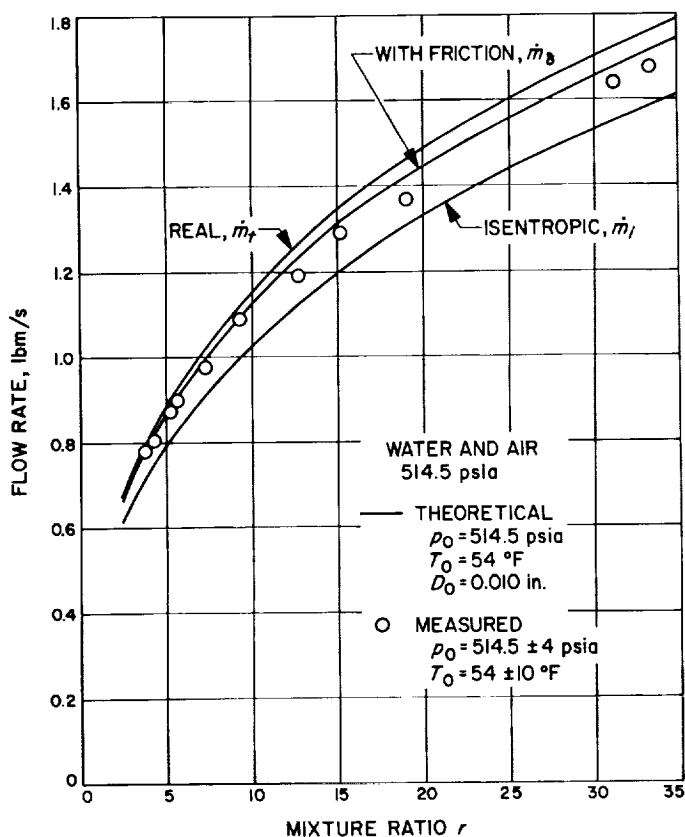


Fig. 35. Comparison of theoretical and experimental flow rates for 6-in. nozzle

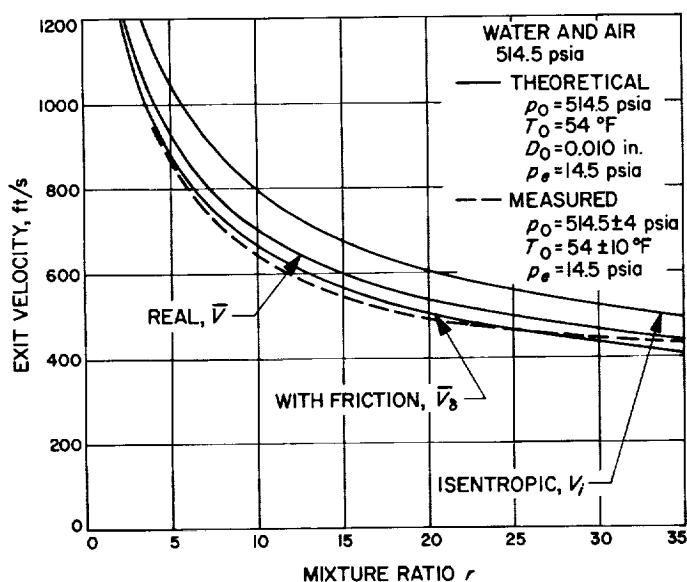


Fig. 36. Comparison of theoretical and experimental exit velocities for 6-in. nozzle

The measured exit velocities range from 3% lower to 3% higher than with the theoretical values (real flow with friction).

#### D. Steam Nozzle

In Ref. 28, flow rates were reported for water-steam mixtures expanding through a converging-diverging nozzle, with the initial quality ranging from zero to 20%. The initial conditions and the measured pressure profile for the runs at 500-psia inlet pressure were supplied to the one-component program using an initial drop diameter of 0.01 in., which was large enough to cause breakup. Figure 37 compares the computed flow rates with the data from Ref. 28 (Fig. 4). The curve is the flow rate with friction; the flow rate without friction is 3% higher. The predicted flow rate is 30% below the measured value at a quality of 1.0%, and 15% below at 3% quality. Agreement is between 1 and 10% at higher qualities. The difference between predicted and measured flow rates at low quality is interpreted as the result of poor uniformity of the flow entering the experimental nozzle at those qualities.

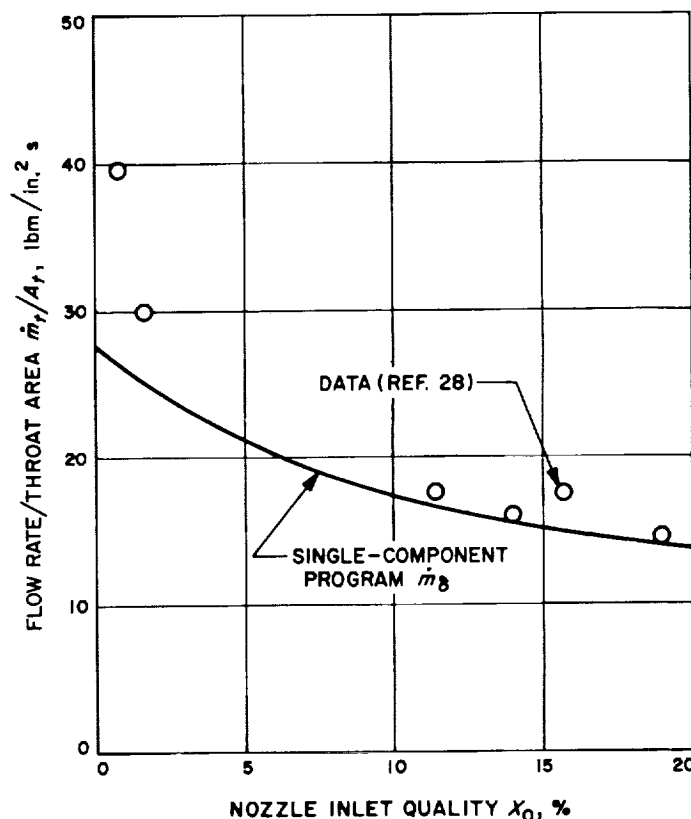


Fig. 37. Comparison of theoretical and experimental flow rates for steam-water nozzle of Ref. 28

### E. Liquid Nitrogen Nozzle

Experiments were reported by Richard (Ref. 29) in which room-temperature nitrogen gas was mixed with liquid nitrogen at the inlet of a two-phase nozzle. The injector provided a uniform spatial distribution of the liquid. The purpose of the experiments was to determine whether any gain in exit velocity over the value for equal gas and liquid temperature could be obtained with the initial temperature of the gas higher than that of the liquid. The measured velocities were such as to indicate that thermal equilibrium was reached on mixing, with no gain from the elevated temperature of the gas.

To obtain nozzle inlet conditions for the one-component program, it was assumed that the injected gaseous and liquid nitrogen streams reached equal velocity and temperature immediately at the exit of the injector at the pressures measured there in the experiments; the pressures ranged from 206 to 289 psia. Under the assumption of thermal equilibrium, the resulting mixture consisted of subcooled liquid nitrogen in all cases. The velocity of the liquid, calculated from the flow rate and nozzle area at the injector exit, ranged from 104 to 114 ft/s. The liquid was then assumed to accelerate in the converging section of the nozzle until the saturation pressure, ranging from 69 to 188 psia, was reached. The corresponding flow areas were all larger than the throat area, but the velocities were such that the first increment of pressure drop below saturation would produce a percentage increase in velocity which was smaller than the percentage increase in volume from vaporization. Thus, the liquid could not vaporize upstream of the throat, and the only flow condition possible with thermal equilibrium was subcooled liquid upstream of the throat, saturated liquid at the throat, and vaporization starting immediately downstream of the throat. The velocity at the throat could then be calculated from the flow rate, liquid density, and throat area. Using this velocity together with saturated liquid nitrogen properties as inlet conditions to the one-component nozzle program, the exit velocity was calculated, and the comparison with Richard's data is shown in Fig. 38. The calculated exit velocity with friction included,  $\bar{V}_8$ , agrees with the measurements within an average deviation of 4.3%. The good agreement is considered to verify both the one-component program as applied to this case and the assumption of thermal equilibrium upstream of the throat in Richard's experiments. Of particular interest is the fact that friction must be included for good agreement and that the friction produces a 14% velocity reduction, the largest of any of the examples considered. The cause is the larger wall area

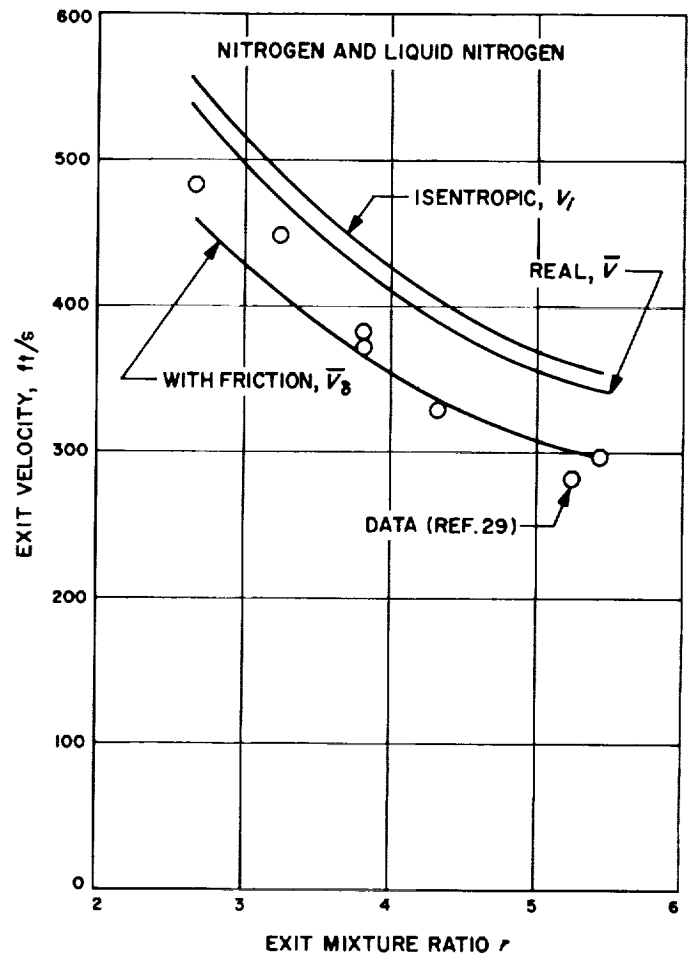


Fig. 38. Comparison of theoretical and experimental exit velocities for liquid nitrogen nozzle of Ref. 29

per unit flow rate and lower average void fraction in the liquid nitrogen nozzle than in the others. Thus, the friction can account for the velocity reduction below isentropic, and it is not necessary to postulate a lag in vaporization as was done by Richard. The free-stream velocity  $\bar{V}$  is only 3.5% below isentropic, because of the high density of the cold gas and the low surface tension of the liquid, resulting in good atomization at a low slip velocity.

### VI. Summary and Conclusions

A one-dimensional analysis of two-phase nozzle flow of liquids and gases was made. The analysis employed five relations: the momentum and energy equations for the mixture, the drag and heat-transfer relations between the phases, and the Weber number = 6 criterion for drop diameter. The latter relation, and the use of the solid-

sphere drag coefficient, were the main simplifications and probably the main source of error in applying the analysis to experimental nozzles; in an actual nozzle, the drops have a range of diameters extending below the Weber number = 6 limit, and the drag coefficient can be higher than for a sphere because of flattening.

Four computer programs were written for computation of real and isentropic flows of single-component and two-component mixtures. The real-flow programs provide the options of a prescribed pressure profile or an optimum pressure profile, and of selecting constant drop diameter or breakup to the Weber number = 6 limit.

Two-phase nozzle design was investigated using the programs. It was found that the optimum nozzle profile has an elongated throat region, that the required shape is insensitive to drop diameter and nozzle length, and that the exit velocity is insensitive to departures from the optimum shape. For given fluids and pressures, the exit velocity was found to be insensitive to nozzle length and flow rate beyond certain minimum values; for water and nitrogen expanding from 150 to 14.1 psia at a mixture ratio of 40, for example, the exit velocity is between 275 and 300 ft/s (78 to 85% of isentropic) for flow rates from 10 to 1000 lbm/s at the optimum lengths; for a flow rate of 160 lb/s, the exit velocity is between 275 and 292 ft/s for all lengths between 5 and 225 in. This insensitivity of nozzle exit velocity to nozzle shape and size results from the inverse dependence of drop size on slip velocity, which apparently acts to adjust the slip to a value that holds the exit velocity in the range 75 to 90%

of isentropic. Thus, it is difficult to design either a very good or a very poor two-phase nozzle.

Theoretical and experimental values of flow rates and exit velocities were compared for two experimental nozzles, 50 and 6 in. long, operating with water and nitrogen, and water and air, respectively. For the large nozzle, the measured flow rates were 3 to 5% lower, and the measured exit velocities 3 to 5% higher, than the predictions. The deviations are attributed to the overestimation of drop diameter and underestimation of drop drag coefficient in the analysis. For the small nozzle, the measured flow rates were 1 to 2% lower, and the measured exit velocities from 3% lower to 3% higher, than the predictions. The closer agreement between measurement and prediction in the small nozzle is attributed to closer equality between the mean and the Weber number = 6 drop size due to shorter time for drop breakup.

Comparisons of theoretical and experimental results for one-component flow were made for two experiments reported in the literature. The theoretical flow rate for a steam nozzle differed from the experimental values by as much as 30%, but the experimental nozzle had no method of ensuring spatially uniform liquid distribution at the inlet, which is a requisite in the theory. The theoretical exit velocity for a two-phase nitrogen nozzle agreed within 5% with the measurements.

It is concluded that the analysis and computation method presented in this report will permit prediction of flow rates and exit velocities to an accuracy of 5% for two-phase nozzles having spatially uniform flow.

## Nomenclature

<i>Symbol</i>	<i>Computer Input or Output Name</i>	<i>Definition</i>
$a$	—	defined by Eq. (11)
$A$	A	flow area, in. <sup>2</sup>
$\bar{A}$	AB	flow area after velocity and temperature equalization, in. <sup>2</sup>
$b$	—	defined by Eq. (12)

<i>Symbol</i>	<i>Computer Input or Output Name</i>	<i>Definition</i>
$c_{ag}$	CAG(P,T)	specific heat of component A gas at pressure $p$ and temperature $T$ , Btu/lbm °R
$c_{al}$	CAL(T)	specific heat of component A liquid, Btu/lbm °R

# Nomenclature (contd)

Symbol	Computer Input or Output Name	Definition	Symbol	Computer Input or Output Name	Definition
$c_{bg}$	CBG(P,T)	specific heat of component <i>B</i> gas at pressure <i>p</i> and temperature <i>T</i> , Btu/lbm °R	$h_g$	HG(P)	enthalpy of saturated vapor at pressure <i>p</i> (single component flow), Btu/lbm
$c_{bl}$	CBL(T)	specific heat of component <i>B</i> liquid, Btu/lbm °R	<i>H</i>	H	inverse Henry's Law constant, in. <sup>2</sup> /lbf
$C_D$	—	drop drag coefficient	$k_{ag}$	KAG(T)	thermal conductivity of component <i>A</i> gas at temperature <i>T</i> , Btu/h ft °R
$C_{Dm}$	CDM	value of $C_D$ at midpoint of a pressure step	$k_{bg}$	KBG(T)	thermal conductivity of component <i>B</i> gas at temperature <i>T</i> , Btu/h ft °R
$C_f$	—	skin-friction coefficient for nozzle wall	$k_g$	KGM	thermal conductivity of gas phase at midpoint of a pressure step, Btu/h ft °R
$C_{fi}$	CFIM	skin-friction coefficient for inside wall of an annular nozzle	<i>L</i>	—	nozzle length, in.
$C_{fl}$	—	skin-friction coefficient for pure liquid flow	<i>L</i>	L(P)	latent heat of vaporization at pressure <i>p</i> (single-component flow), Btu/lbm
$C_{fo}$	CFOM	skin-friction coefficient for wall of a circular nozzle or for outside wall of an annular nozzle	$L_a$	LA(T)	latent heat of vaporization of component <i>A</i> at temperature <i>T</i> , Btu/lbm
$c_g$	—	specific heat of gas, Btu/lbm °R	$L_b$	LB(T)	latent heat of vaporization of component <i>B</i> at temperature <i>T</i> , Btu/lbm
$c_{gm}$	CGM	specific heat of gas at the midpoint of a pressure step, Btu/lbm °R	$L_m$	LM	latent heat of vaporization at midpoint of a pressure step (single-component flow, Btu/lbm)
$c_l$	—	specific heat of liquid, Btu/lbm °R	$\dot{m}_a$	—	flow rate of component <i>A</i> , lbm/s
$c_l$	CL(P)	specific heat of saturated liquid at pressure <i>p</i> (single-component flow), Btu/lbm °R	$\dot{m}_{ag}$	—	flow rate of component <i>A</i> gas, lbm/s
$c_{lm}$	CLM	specific heat of liquid at the midpoint of a pressure step, Btu/lbm °R	$\dot{m}_{al}$	—	flow rate of dissolved component <i>A</i> , lbm/s
<i>D</i>	D	drop diameter, in.	$\dot{m}_b$	—	flow rate of component <i>B</i> , lbm/s
$D_{max}$	—	maximum drop diameter, corresponding to $We = 6$ , in.	$\dot{m}_{bg}$	—	flow rate of component <i>B</i> gas, lbm/s
$D_0$	DO	initial drop diameter, in.	$\dot{m}_{bl}$	—	flow rate of dissolved component <i>B</i> , lbm/s
$F_d$	—	drag force on liquid, lbf			
<i>h</i>	HM	heat-transfer coefficient between gas and drops at midpoint of a pressure step, Btu/h ft <sup>2</sup>			

## Nomenclature (contd)

Symbol	Computer Input or Output Name	Definition	Symbol	Computer Input or Output Name	Definition
$\dot{m}_g$	MG	gas flow rate, lbm/s	$r_c$	RC	ratio of component B mass flow rate to component A mass flow rate
$\bar{\dot{m}}_g$	MGB	gas flow rate after velocity and temperature equalization, lbm/s	$r_v$	RV	ratio of gas volume flow rate to liquid volume flow rate
$\dot{m}_i$	—	isentropic total flow rate, lbm/s	$\bar{r}_v$	RVB	ratio of gas volume flow rate to liquid volume flow rate after velocity and temperature equalization
$\dot{m}_l$	ML	liquid flow rate, lbm/s	$R$	—	universal gas constant, 10.732 (lbm/ft <sup>3</sup> )/lb-mole °R
$\bar{\dot{m}}_l$	MLB	liquid flow rate after velocity and temperature equalization, lbm/s	$Re$	REM	Reynolds number for drop motion relative to gas at midpoint of a pressure step, $\rho_g D  V_s  / \mu_g$
$\dot{m}_t$	EMT	total flow rate, lbm/s	$Re_f$	REF	Reynolds number for liquid film flow at midpoint of a separator
$\dot{m}_\delta$	—	flow rate corrected for boundary layer at throat, lbm/s	$R_i$	—	radius from axis to inner wall of an annular nozzle, in.
$\dot{M}$	—	momentum flux, lbm ft/s <sup>2</sup>	$R_o$	—	radius from axis to outer wall of an annular nozzle, in.
$\dot{N}$	—	number flow rate of drops, s <sup>-1</sup>	$R_{\delta_o}$	REDOM	Reynolds number based on velocity boundary layer thickness at wall of a circular nozzle or on outside wall of an annular nozzle at midpoint of a pressure step
$p$	P	pressure, lbf/in. <sup>2</sup>	$R_{\delta_i}$	REDIM	Reynolds number based on velocity boundary layer thickness on inside wall of an annular nozzle
$p_a$	PA	partial pressure of component A, lbf/in. <sup>2</sup>	$R_\phi$	—	radius from axis to flow centerline of an annular nozzle, in.
$\bar{p}_a$	PAB	partial pressure of component A after velocity and temperature equalization, lbf/in. <sup>2</sup>	$R_{\phi_o}$	RAXO	value of $R_\phi$ at nozzle inlet, in.
$p_b$	PB	partial pressure of component B, lbf/in. <sup>2</sup>	$s$	S	ratio of slip velocity to mean velocity $V_s/\bar{V}$
$\bar{p}_b$	PBB	partial pressure of component B after velocity and temperature equalization, lbf/in. <sup>2</sup>	$s_o$	—	optimum value of slip $s$
$p_{b_o}$	PBO(T)	vapor pressure of pure component B at temperature $T$ , lbf/in. <sup>2</sup>	$S_a$	SA	Sutherland constant for component A, °R
$Q$	Q	separator parameter defined by Eq. (123)	$S_b$	SB	Sutherland constant for component B, °R
$r$	R	ratio of liquid mass flow rate to gas mass flow rate			
$\bar{r}$	RB	value of $r$ after velocity and temperature equalization			
$r_a$	RA	ratio of gas flow area to liquid flow area, $\rho_l V_l / r \rho_g V_g$			

## Nomenclature (contd)

Symbol	Computer Input or Output Name	Definition	Symbol	Computer Input or Output Name	Definition
$T$	T(P)	saturation temperature at pressure $p$ (single component flow), °R	$W_{a_i}$	WAL	molecular weight of component A
$\bar{T}$	TB	temperature after velocity and temperature equalization, °R	$W_{b_g}$	WBG(P,T)	effective molecular weight of component B gas at pressure $p$ and temperature $T$
$T_g$	TG	gas temperature, °R	$\bar{W}_{b_g}$	WBGB	effective molecular weight of component B gas after velocity and temperature equalization
$T_{g_0}$	TGO	temperature of gas at nozzle inlet, °R	$W_{b_i}$	WBL	molecular weight of component B
$T_l$	TL	liquid temperature, °R	$We$	—	Weber number, $\rho_g V_g^2 D / 2\sigma$
$T_{l_0}$	TLO	temperature of liquid at nozzle inlet, °R	$W_g$	WG	effective molecular weight of gas
$T_0$	TO	temperature at nozzle inlet (isentropic flow), °R	$\bar{W}_g$	WGB	effective molecular weight of the gas after velocity and temperature equalization
$\dot{v}_{a_i}$	—	volume flow rate of component A liquid, ft <sup>3</sup> /s	$x$	X	axial distance from nozzle inlet, in.
$\dot{v}_{b_i}$	—	volume flow rate of component B liquid, ft <sup>3</sup> /s	$X_g$	XG	quality $\dot{m}_g / \dot{m}_i$
$\dot{v}_g$	—	volume flow rate of gas, ft <sup>3</sup> /s	$\bar{X}_g$	XGB	quality after velocity and temperature equalization
$V$	V	velocity (isentropic flow), ft/s	$X_{g_0}$	XGO	quality at inlet of nozzle
$\bar{V}$	VB	mean velocity $(V_g + rV_l)/(1 + r)$ , ft/s	$y_i$	YI	distance from flow centerline to inner wall of an annular nozzle, in.
$V_g$	VG	gas velocity, ft/s	$y_0$	YO	radius of circular nozzle, or distance from flow centerline to outer wall of an annular nozzle, in.
$V_{g_0}$	VGO	gas velocity at nozzle inlet, ft/s	$\alpha$	ALPHA	mass fraction of component A dissolved in liquid
$V_l$	VL	liquid velocity, ft/s	$\bar{\alpha}$	ALPHB	mass fraction of component A dissolved in liquid after velocity and temperature equalization
$V_{l_0}$	VLO	liquid velocity at nozzle inlet, ft/s	$\beta$	BETA	mass fraction of component B vapor in gas
$V_s$	VS	slip velocity $V_g - V_l$ , ft/s	$\bar{\beta}$	BETAB	mass fraction of component B vapor in gas after velocity and temperature equalization
$\bar{V}_\delta$	VBD	mean velocity including boundary layer, ft/s	$\delta$	—	velocity thickness of boundary layer, in.
$V_0$	VO	velocity at nozzle inlet (isentropic flow), ft/s			
$W_{a_g}$	WAG(P,T)	effective molecular weight of component A gas at pressure $p$ and temperature $T$			
$\bar{W}_{a_g}$	WAGB	effective molecular weight of component A gas after velocity and temperature equalization			

## Nomenclature (contd)

<i>Symbol</i>	<i>Computer Input or Output Name</i>	<i>Definition</i>	<i>Symbol</i>	<i>Computer Input or Output Name</i>	<i>Definition</i>
$\delta^*$	—	displacement thickness of the boundary layer, in.	$\Delta r$	—	change in $r$ across a pressure step
$\delta_i$	DELI	velocity thickness of boundary layer on the inner wall of an annular nozzle, in.	$\Delta s$	—	change in slip across a pressure step
$\delta_i^*$	DELSI	displacement boundary layer thickness on inside wall of an annular nozzle, in.	$\Delta T_g$	—	change in gas temperature across a pressure step, °R
$\delta_m T$	—	difference between $T_g$ and $T_l$ at midpoint of a pressure step, °R	$\overline{\Delta T_g}$	—	change in gas temperature due to velocity and temperature equalization, °R
$\delta_o$	DELO	velocity thickness of boundary layer on wall of a circular nozzle or on outer wall of an annular nozzle, in.	$\Delta T_l$	—	change in liquid temperature across a pressure step, °R
$\delta_o^*$	DELISO	displacement boundary layer thickness on wall of a circular nozzle or on outer wall of an annular nozzle, in.	$\overline{\Delta T_l}$	—	change in liquid temperature due to velocity and temperature equalization, °R
$\delta_i T$	—	difference between $T_g$ and $T_l$ at beginning of a pressure step, °R	$\Delta \bar{V}^2$	—	change in square of mean velocity across a pressure step, ft <sup>2</sup> /s <sup>2</sup>
$\delta_i V^2$	—	difference between $V_g^2$ and $V_l^2$ at beginning of a pressure step, ft <sup>2</sup> /s <sup>2</sup>	$\Delta V_g^2$	—	change in $V_g^2$ across a pressure step, ft <sup>2</sup> /s <sup>2</sup>
$\delta T$	—	difference between $T_g$ and $T_l$	$\Delta V_l^2$	—	change in $V_l^2$ across a pressure step, ft <sup>2</sup> /s <sup>2</sup>
$\Delta A$	—	change in flow area across a pressure step, in. <sup>2</sup>	$\Delta x$	—	change in $x$ across a pressure step, in.
$\Delta H_n$	—	change in enthalpy across a pressure step for process $n$ , Btu/lbm °R	$\theta$	—	momentum thickness of boundary layer, in.
$\Delta \dot{m}_{a_g}$	—	change in flow rate of component $A$ gas across a pressure step, lbm/s	$\theta_i$	THI	momentum boundary layer thickness on inside wall of an annular nozzle, in.
$\Delta \dot{m}_{b_g}$	—	change in flow rate of component $B$ gas across a pressure step, lbm/s	$\theta_{i_0}$	THIO	initial momentum boundary layer thickness on inside wall of an annular nozzle, in.
$\Delta \dot{m}_g$	—	change in gas flow rate across a pressure step, lbm/s	$\theta_o$	THO	momentum boundary layer thickness on wall of a circular nozzle or on outer wall of an annular nozzle, in.
$\Delta p$	DP	pressure change in one pressure step, lbf/in. <sup>2</sup>	$\theta_{o_0}$	THOO	initial momentum boundary layer thickness on wall of a circular nozzle or on outer wall of an annular nozzle, in.

## Nomenclature (contd)

<i>Symbol</i>	<i>Computer Input or Output Name</i>	<i>Definition</i>	<i>Symbol</i>	<i>Computer Input or Output Name</i>	<i>Definition</i>
$\lambda$	ALAM	Lagrangian multiplier for nozzle contour optimization, ft/s <sup>2</sup>	$\rho_l$	ROL(P)	density of saturated liquid (single-component flow), lbm/ft <sup>3</sup>
$\mu_{a_g}$	VIAG(T)	viscosity of component A gas at temperature $T$ , lbm/ft h	$\bar{\rho}_l$	ROLB	density of liquid after velocity and temperature equalization, lbm/ft <sup>3</sup>
$\mu_{a_l}$	VIAL(T)	viscosity of component A liquid at temperature $T$ , lbm/ft h	$\rho_{l_m}$	ROLM	density of liquid at midpoint of a pressure step, lbm/ft <sup>3</sup>
$\mu_{b_g}$	VIBG(T)	viscosity of component B gas at temperature $T$ , lbm/ft h	$\sigma$	SIGMA	surface tension of liquid, dyn/cm
$\mu_{b_l}$	VIBL(T)	viscosity of component B liquid at temperature $T$ , lbm/ft h	$\sigma$	SIG(P)	surface tension of saturated liquid at pressure $p$ (single-component flow), dyn/cm
$\mu_g$	VIG(P)	viscosity of saturated vapor at pressure $p$ (single-component flow), lbm/ft h	$\sigma$	SIG(T)	surface tension of component B liquid at temperature $T$ , dyn/cm
$\mu_g$	VIGM	viscosity of gas at midpoint of pressure step, lbm/ft h	$\tau_{w_i}$	TWIM	shear on inner wall of an annular nozzle, lbf/in. <sup>2</sup>
$\mu_l$	VIL(P)	viscosity of saturated liquid at pressure $p$ (single-component flow), lbm/ft h	$\tau_{w_o}$	TWOM	shear on wall of a circular nozzle or on outer wall of an annular nozzle, lbf/in. <sup>2</sup>
$\mu_l$	VILM	viscosity of liquid at midpoint of a pressure step, lbm/ft h	$\phi$	PHI	angle between axis and flow centerline of an annular nozzle, deg
$\bar{\mu}_l$	VILB	viscosity of liquid after velocity and temperature equalization, lbm/ft h	$\omega_i$	WIM	angle of inner wall relative to flow centerline for an annular nozzle, deg
$\rho_{a_l}$	ROAL(T)	density of component A liquid at temperature $T$ , lbm/ft <sup>3</sup>	$\omega_o$	WOM	angle of wall relative to axis for a circular nozzle, or angle of outer wall relative to flow centerline for an annular nozzle, deg
$\rho_{b_l}$	ROBL(T)	density of component B liquid at temperature $T$ , lbm/ft <sup>3</sup>	<b>Subscripts</b>		
$\rho_g$	ROG	density of gas, lbm/ft <sup>3</sup>	$e$		nozzle exit
$\rho_g$	ROG(P)	density of saturated vapor (single-component flow), lbm/ft <sup>3</sup>	$i$		isentropic flow
$\bar{\rho}_g$	ROGB	density of gas after velocity and temperature equalization, lbm/ft <sup>3</sup>	$m$		midpoint of a pressure step
$\rho_{g_m}$	ROGM	density of gas at midpoint of a pressure step, lbm/ft <sup>3</sup>	$t$		nozzle throat
$\rho_l$	ROL	density of liquid, lbm/ft <sup>3</sup>	0		nozzle inlet
			1		beginning of a pressure step
			2		end of a pressure step



## References

1. Elliott, D. G., *Theoretical and Experimental Investigation of a Gas-Driven Jet Pump for Rocket Engines*, Report No. I-58-3. Jet Propulsion Center, School of Mechanical Engineering, Purdue University, Lafayette, Ind., Dec. 1958; also in *Liquid Rockets and Propellants, Progress in Astronautics and Rocketry—Volume 2*, pp. 497–541. Academic Press, New York, 1960.
2. Crabtree, D. L., *Investigation of a Gas-Driven Jet Pump for Rocket Engines*, Report No. F-62-1. Jet Propulsion Center, School of Mechanical Engineering, Purdue University, Lafayette, Ind., Jan. 1962.
3. Elliott, D. G., Cerini, D. J., and Weinberg, E., "Liquid-Metal MHD Power Conversion," *Space Power Systems Engineering*, pp. 1275–1297. Academic Press Inc., New York, 1966.
4. Elliott, D. G., "Magnetohydrodynamic Power Systems," *J. Spacecraft and Rockets*, Vol. 4, No. 7, pp. 842–846, 1967; also Technical Report 32-1129. Jet Propulsion Laboratory, Pasadena, Calif., July 1967.
5. Tangren, R. F., Dodge, C. H., and Seifert, H. S., "Compressibility Effects in Two-Phase Flow," *J. Applied Physics*, Vol. 20, No. 7, pp. 637–645, 1949.
6. Kliegel, J. R., *One Dimensional Flow of a Gas-Particle System*. Report No. TR-59-0000-00746, Space Technology Laboratories, Los Angeles, Calif., July 1959; also, IAS Paper No. 60-5, American Institute of Aeronautics and Astronautics, New York, Jan. 1960.
7. Crabtree, D. L., *Investigation of the Influence of the Design Parameters on the Flow Characteristics of the Drive Nozzle of a Gas-Driven Jet Pump*, MS Thesis, School of Mechanical Engineering, Purdue University, Lafayette, Ind., Aug. 1961.
8. Netzer, D. W., *Calculations of Flow Characteristics for Two-Phase Flow in Annular Converging-Diverging Nozzles*, Report No. TM-62-3. Jet Propulsion Center, School of Mechanical Engineering, Purdue University, Lafayette, Ind., June 1962.
9. Elliott, D. G., "Analysis of the Acceleration of Lithium in a Two Phase Nozzle," *Proceedings of the 1963 High Temperature Liquid Metal Heat Transfer Technology Meeting*, pp. 353–370. Oak Ridge National Laboratory, Oak Ridge, Tenn., Dec. 1964.
10. Hanson, A. R., Domich, E. G., and Adams, H. S., "Shock Tube Investigation of the Breakup of Drops by Air Blasts," *Physics of Fluids*, Vol. 6, No. 8, pp. 1070–1080, 1963.
11. Morrell, G., *Critical Conditions for Drop and Jet Shattering*, NASA TN D-677. National Aeronautics and Space Administration, Washington, Feb. 1961.

## References (contd)

12. El Wakil, M. M., Priem, R. J., Brikowski, H. J., Myers, P. S., and Uyehara, O. A., *Experimental and Calculated Temperature and Mass Histories of Vaporizing Fuel Drops*, NASA TN 3490. National Aeronautics and Space Administration, Washington, Jan. 1956.
13. Shapiro, A. H., *The Dynamics and Thermodynamics of Compressible Fluid Flow*, Vol. I. The Ronald Press Company, New York, 1953.
14. Hougen, O. A., Watson, K. M., and Ragatz, R. A., *Chemical Process Principles (Part I, Material and Energy Balances)*, Second Edition. John Wiley & Sons, Inc., New York, 1954.
15. Eckert, E. R. G., and Drake, R. M., *Heat and Mass Transfer*. McGraw-Hill Book Company, Inc., New York, 1959.
16. Stonecypher, T. E., *Dynamic and Thermal Non-Equilibrium in Two-Phase Flow in Rocket Nozzles*. Report No. P-60-17. Rohm and Haas Company, Huntsville, Alabama, December 1960.
17. Perry, J. H., Chilton, C. H., and Kirkpatrick, S. O., *Chemical Engineers' Handbook*, 4th Edition, McGraw-Hill Book Co., Inc., New York, 1963.
18. Ingebo, R. D., *Drag Coefficients for Droplets and Solid Spheres in Clouds Accelerating in Air Streams*, NASA TN 3762, National Aeronautics and Space Administration, Washington, Sept. 1956.
19. Hughes, R. R., and Gilliland, E. R., "The Mechanics of Drops," *Chem. Eng. Prog.*, Vol. 48, No. 10, pp. 497-504, Oct. 1952.
20. Rabin, E., Schallenmuller, A. R., and Lawhead, R. B., *Displacement and Shattering of Propellant Droplets*, Report No. AFOSR TR 60-75. Air Force Office of Scientific Research, Washington, Mar. 1960.
21. Kreith, F., *Principles of Heat Transfer*, Second Edition. International Textbook Company, Scranton, Pa., 1965.
22. Courant, R., and Hilbert, D., *Methods of Mathematical Physics*, Vol. 1. Interscience Publishers, Inc., New York, 1953.
23. Marble, F. E., "Nozzle Contours for Minimum Particle-Lag Loss," *AIAA J.*, Vol. 1, No. 12, pp. 2793-2801, 1963.
24. Elliott, D. G., Bartz, D. R., and Silver, S., *Calculation of Turbulent Boundary-Layer Growth and Heat Transfer in Axi-Symmetric Nozzles*, Technical Report 32-387. Jet Propulsion Laboratory, Pasadena, Calif., Feb. 1963.
25. Eddington, R. B., *Investigation of Supersonic Shock Phenomena in a Two-Phase (Liquid-Gas) Tunnel*, Technical Report 32-1096. Jet Propulsion Laboratory, Pasadena, Calif., Mar. 1967; also, AIAA Paper No. 66-87, American Institute of Aeronautics and Astronautics, New York, Jan. 1966.

### References (contd)

26. Elliott, D., Cerini, D., O'Connor, D., and Weinberg, E., *Liquid MHD Power Conversion*, Space Programs Summary 37-27, Vol. IV, pp. 75-83. Jet Propulsion Laboratory, Pasadena, Calif., June 1964.
27. Weinberg, E., and Hays, L. G., *Comparison of Liquid-Metal Magnetohydrodynamic Power Conversion Cycles*, Technical Report 32-946. Jet Propulsion Laboratory, Pasadena, Calif., Aug. 15, 1966.
28. Starkman, E. S., Schrock, V. E., Neusen, K. F., and Mancely, D. J., "Expansion of a Very Low Quality Two-Phase Fluid Through a Convergent-Divergent Nozzle," Paper No. 63-AHGT-4, American Society of Mechanical Engineers, New York, Mar. 1963.
29. Richard, L. P., *The Effect of an Initially Large Internal Temperature Difference, and Condensibility of the Gas, on the Exit Velocity for Two-Phase Flow of a Liquid and a Gas in a Nozzle*, MS Thesis, School of Mechanical Engineering, Purdue University, Lafayette, Ind., Aug. 1959; also Reese, B. A., and Richard, L. P., "Equilibrium Between Phases in Converging-Diverging Nozzles," ARS Paper No. 1714-61, American Institute of Aeronautics and Astronautics, New York, Apr. 1961.

